

Identification of Thermally-Tagged Coherent Structures in the Zero Pressure Gradient Turbulent Boundary Layer

Thesis by
Rebecca Rought

In Partial Fulfillment of the Requirements
for the Degree of Engineer



California Institute of Technology
Pasadena, California

2013

©2013

Rebecca Rought

All Rights Reserved

Acknowledgements

This research was made possible by the Air Force Office of Scientific Research, grant # FA9550-09-1-0701. In addition, I would like to thank my advisor, Beverley McKeon, for her support with this project. The GALCIT support staff, especially everyone in the Aero shop, was a tremendous help in completing this research. The help of Stanislav Gordeyev with setting up and understanding the Malley probe is also appreciated. I would also like to thank Edward Guzman for his help in developing the layout of the Malley probe used in this experiment.

Abstract

A zero pressure gradient boundary layer over a flat plate is subjected to step changes in thermal condition at the wall, causing the formation of internal, heated layers. The resulting temperature fluctuations and their corresponding density variations are associated with turbulent coherent structures. Aero-optical distortion occurs when light passes through the boundary layer, encountering the changing index of refraction resulting from the density variations. Instantaneous measurements of streamwise velocity, temperature and the optical deflection angle experienced by a laser traversing the boundary layer are made using hot and cold wires and a Malley probe, respectively. Correlations of the deflection angle with the temperature and velocity records suggest that the dominant contribution to the deflection angle comes from thermally-tagged structures in the outer boundary layer with a convective velocity of approximately $0.8U_\infty$. An examination of instantaneous temperature and velocity and their temporal gradients conditionally averaged around significant optical deflections shows behavior consistent with the passage of a heated vortex. Strong deflections are associated with strong negative temperature gradients, and strong positive velocity gradients where the sign of the streamwise velocity fluctuation changes. The power density spectrum of the optical deflections reveals associated structure size to be on the order of the boundary layer thickness. A comparison to the temperature and velocity spectra suggests that the responsible structures are smaller vortices in the outer boundary layer as opposed to larger scale motions. Notable differences between the power density spectra of the optical deflections and the temperature remain unresolved due to the low frequency response of the cold wire.

Contents

1	Introduction	1
1.1	Turbulent Boundary Layer Structure	1
1.2	Thermally Perturbed Boundary Layers	5
1.3	Aero-Optical Properties of Turbulence	7
2	Experimental Setup	10
2.1	Wind Tunnel Facility	10
2.2	Plate setup	11
2.3	The Heating System	13
2.4	Flow Measurements	15
2.5	Temperature Measurements	17
2.6	Malley Probe Measurements	18
2.7	Measurement Locations	22
3	Results	23
3.1	Flow Characteristics	23
3.2	Mean Convective Velocity	27
3.3	Correlation of Deflection Angle and Flow Properties	29
3.4	Power Density Spectra	33
3.5	Conditional Averaging	36
4	Conclusion	41
4.1	Main Results	41
4.2	Limitations	42
4.3	Future Work	43

List of Figures

1.1	Hairpin Packets Proposed by Adrian et al. (2000)	4
2.1	Merrill Wind Tunnel Test Section	10
2.2	Plate Layout	11
2.3	Measurement Section with Pitot Tube	13
2.4	Temperature Distribution of Plate from IR Camera, Color bar in °F	13
2.5	Plate Temperature Distribution Obtained by RTD Probe	14
2.6	Plate Streamwise Temperature Gradient	14
2.7	Original and Corrected Hot Wire Calibration Curves	16
2.8	Cold Wire Calibration Curve	18
2.9	Principle Parts of Malley Probe	19
2.10	Deflection angle calculation	19
2.11	Malley Probe Setup	19
2.12	PSD Calibration Curves	21
2.13	Power Density Spectra of Lasers in No Flow Case	22
2.14	Location of Measurements Relative to One Another.	22
3.1	Mean Velocity Profile, Inner Scaling	23
3.2	Turbulence Intensities	24
3.3	Skew and Kurtosis of Velocity	25
3.4	Mean Temperature Profiles	25
3.5	Fluctuating Temperature Profiles	26
3.6	Growth in the Boundary Layer and Internal Layer Between Measurement Points	26
3.7	Deflection Angle Spectra from the Two Beams	28
3.8	Argument of Spectral Correlation Function vs. Frequency	28
3.9	Correlation of θ_1 and θ_2	29
3.10	(a) Correlation of Temperature and Optical Distortion (b) Temperature Fluctuations	30

3.11 (a) Temperature Skew (b) Temperature Kurtosis	31
3.12 Correlation of Velocity and Deflection Angle	31
3.13 Correlation of Deflection Angle and (a) Temperature at $y^+ = 139$ (b) Velocity at $y^+ = 170$	33
3.14 Temperature, Velocity, and Deflection Spectra	34
3.15 Temperature and Velocity Spectra at Different Wall Normal Locations	35
3.16 Spectra of higher moment fluctuations at $y^+ = 139$ of (a) Temperature (b) Velocity	35
3.17 Deflection Angle Spectrum vs Strouhal Number	36
3.18 PDF of (a) Temperature at $y^+ = 114$ (b) Deflection angle	37
3.19 Time Traces at $y^+ = 139$	37
3.20 Fluctuations of T , dT/dt , θ_1 and θ_2	38
3.21 Temperature and Deflection Angle Fluctuations at $y^+ = 52$	39
3.22 Time Traces at $y^+ = 170$	39

Nomenclature

Re	Reynolds Number
U_∞	Free Stream Velocity
ν	Kinematic Viscosity
u_τ	Friction Velocity
y^+	Wall Normal Location
U	Mean Streamwise Velocity
δ	Boundary Layer Thickness
δ^*	Displacement Thickness
δ_θ	Momentum Thickness
u	Streamwise Velocity Fluctuation
U_c	Mean Convective Velocity
k	Wave Number
f	Frequency
θ	Deflection Angle
ϕ	Power Density Spectrum
T_∞	Free Stream Temperature
T_{wh}	Temperature of Plate 1 Surface
T	Local Temperature
δ_T	Internal Layer Thickness
T_τ	Friction Temperature
T^*	Non-Dimensionalized Temperature Difference between T_{wh} and T
T'	Temperature Fluctuations

Chapter 1

Introduction

1.1 Turbulent Boundary Layer Structure

The study of turbulence has a history stretching back to the works of Leonard da Vinci, whose notebooks included sketches of turbulent vortices, with the accompanying description, “observe the motion of the surface of the water which resembles that of hair, and has two motions, of which one goes on with the flow of the surface and the other forms the lines of the eddies ” (Da Vinci and Suh, 2009). A mathematical description of the behavior of fluids wasn’t developed until the mid-1800’s when the Navier-Stokes equations were derived. Early work in understanding turbulence was conducted by Reynolds (1883) who used dye visualizations to study the transition between laminar and turbulent flows. The Reynolds number, which represents the ratio of inertial to viscous forces in the flow, was developed based on these experiments, $Re = \frac{UL}{\nu}$, where U is the velocity of the flow, L is a characteristic length scale, and ν is the kinematic viscosity. When the Reynolds number increases past a critical value, the viscous forces are no longer sufficient to dampen small instabilities in the flow arising from sources such as wall roughness. As a result, a flow will become unstable and transition from laminar to turbulent. It is possible to force a lower Reynolds number flow into turbulence using a tripping mechanism to introduce large instabilities into the flow. Prandtl (1904) first introduced the idea of the boundary layer, describing the effects of friction on the region of a flow adjacent to the wall. Early work describing the behavior of the boundary layer focused on statistical properties and the development of equations to describe the mean flow characteristics. Later studies examined the turbulent structure of the boundary layer, relating statistical observations with individual coherent structures in the flow. The turbulent boundary layer has been widely studied, and only a brief overview of the most relevant topics are discussed here.

Statistical Analysis

The properties of the boundary layer can be described using inner and outer scales. In the region of the boundary layer closest to the wall, the effect of viscosity dominates and the flow is dependent on the wall shear stress, τ_w , fluid density, ρ , and the fluid viscosity, μ . Inner units are non-dimensionalized using the friction velocity $u_\tau = \sqrt{\frac{\tau_w}{\rho}}$. The mean velocity is given as $U^+ = U/u_\tau$, and the wall normal distance $y^+ = yu_\tau/\nu$, where $\nu = \mu/\rho$ is the kinematic viscosity. Outer scaling uses global flow properties and is free from the effects of viscosity. The outer velocity scale also uses u_τ , although is usually written as a velocity deficit from the free stream velocity. The outer length scale is based on the boundary length thickness, δ , displacement thickness, δ^* , or momentum thickness, δ_θ . The most commonly used length scale is δ , which is the thickness where $U = 0.99U_\infty$. The displacement thickness measures the distance the wall would need to move in order for the mass flow rate to be the same as an inviscid fluid and is defined as

$$\delta^* = \int_0^\infty \left(1 - \frac{U(y)}{U_\infty}\right) dy \quad (1.1)$$

The momentum thickness is distance the wall would need to be shifted in order for the fluid to have the same momentum as an inviscid flow,

$$\delta_\theta = \int_0^\infty \frac{U(y)}{U_\infty} \left(1 - \frac{U(y)}{U_\infty}\right) dy \quad (1.2)$$

The boundary layer can be separated into different regions where different flow variables control the mean velocity profile. A description of these regions is outlined in Tennekes and Lumley (1972). Closest to the wall, where $y^+ < 5$ is the viscous sublayer. In this layer, viscous effects dominate and the mean velocity profile can be described as $U^+ = y^+$. The buffer layer is located between the viscous sublayer and the inertial sublayer. In this region both the viscous stresses and the Reynolds stresses are important. The Reynolds stresses are inertial stresses associated with turbulent velocity fluctuations, $\tau_{ij} = -\overline{\rho u_i u_j}$, where u, v , are fluctuating velocity components. In the inertial sublayer, the Reynolds stresses dominate and the mean velocity profile follows the law of the wall,

$$U^+ = 1/\kappa \ln(y^+) + B \quad (1.3)$$

Here κ is the von Kármán number and the values of κ and B are dependent on the flow type studied. For a zero pressure gradient turbulent boundary layer, $\kappa = 0.384$ and $B = 4.17$, based on the work by Nagib et al (2007). The wall shear stress can be found by matching the mean velocity profile to the law of the wall (Clauser 1956). Above the log region, in the outer boundary

layer is the wake region. Coles (1956) defined the law of the wake to determine the velocity in this region,

$$U^+ = f(y^+) + \frac{\Pi}{\kappa} W\left(\frac{y}{\delta}\right) \quad (1.4)$$

Here Π is the wake parameter and $W(\frac{y}{\delta})$ is the wake function. For a more in depth discussion of these regions of the boundary layer see the review paper by Cantwell (1981), or for scaling arguments in the boundary layer, DeGraaff and Eaton (2000).

High order streamwise statistics are useful in understanding the behavior of a turbulent flow. The turbulence intensities are given in inner units as $u^+ = u_{rms}/u_\tau$, where u is the difference between the mean and instantaneous streamwise velocity. Streamwise turbulence intensity peaks close to the wall, at $y^+ \approx 15$. The third moment velocity statistics are used to find the skew of a flow, $S_u = \overline{u^3}/u_{rms}^3$. The skew represents the asymmetry of the velocity fluctuations in the flow. The fourth moment velocity statistics represent the kurtosis, $K_u = \overline{u^4}/u_{rms}^4$, or the peakiness of the velocity fluctuations. The velocity power density spectrum at circular frequency ω is useful in determining the size of the most energetic structures in the flow. The power spectral density is the energetic contributions to the mean square of the velocity signal from frequencies between $\omega \pm d\omega$. The frequency spectra can be converted into wave number space by assuming that the coherent structures convect at a velocity equal to the local mean and applying Taylor's hypothesis of frozen flow. Taylor's hypothesis states that, within a small amount of time, the properties of turbulence can be assumed to be unchanging, or frozen. Time can therefore be related to streamwise distance, $t = x/U_c$, where U_c is the convective velocity of the turbulent structures. The wave number is then expressed as $k = 2\pi f/U_c$, and the wavelength is $\lambda = 2\pi/k$. When the pre-multiplied spectrum, $\phi(k) = kE(k)$, is examined graphically using logarithmic scaling, the area under the curve corresponds to the turbulent kinetic energy of the flow contributed by those wave numbers.

Coherent Structures in Turbulence

Robinson (1991) described a coherent structure in turbulence as “a three-dimensional region of the flow over which at least one fundamental flow variable (velocity component, density, temperature, etc.) exhibits significant correlation with itself or with another variable over a range of space and/or time that is significantly larger than the smallest local scales of the flow”. One of the first models of a coherent structure was a hairpin vortex inclined at a 45° angle proposed by Theodorsen in 1952.

Many early studies focused on the “bursting” phenomenon, a term which has been used by different authors to describe a variety of related observations involving the production of turbulence. It describes an explosive event which is associated with an upstream “sweep” and

downstream “ejection”. These events have been studied using quadrant analysis, which defines velocity fluctuations in a uv plane divided into four regions. The fourth quadrant, Q4, contains positive streamwise, negative wall normal velocity fluctuations, which characterize sweeps. Sweeps occur when high speed fluid is brought in towards the wall from the outer boundary layer region. The second quadrant, Q2, represents ejections, which occur when low speed fluid is pushed away from the wall. The presence of an ejection is indicated by a negative streamwise, positive wall normal velocity fluctuation. The presence of Q2 events have been observed to be immediately followed by Q4 events, and tend to occur in sequences of increasingly strong ejections (Bogard and Tiederman 1986).

The behavior of sweeps and ejections was studied using temperature contamination as a passive scalar by Chen and Blackwelder (1978). Their experiment examined the boundary layer developing over a plate which was uniformly heated so that $T_\infty - T_w = 12.8$ °C, thus allowing the fluid near the wall to be warmer than the fluid in the free stream. Using temperature measurements, they were able to study organized motions within the boundary layer. This study examined the large scale turbulent bulges in the outer boundary layer, between which irrotational fluid from outside of the boundary layer could be observed. Flow visualization studies of this phenomenon by Falco (1977) showed these bulges and what appeared to be inclined hairpin vortices on top of the bulges. Robinson (1991) suggested that the bursting phenomena are related to the passage of inclined quasi-streamwise vortices. These vortices cause low speed fluid to be ejected away from the wall by vortex induction. Robinson found quasi-streamwise vortices dominating the buffer layer and arch vortices dominating the wake region, with an equal mixture of these vortices in the logarithmic region.

A model of the boundary layer incorporating these observations was proposed by Adrian et al. (2000), who suggested that the main structure in the boundary layer is the hairpin packet, shown in Figure 1.1

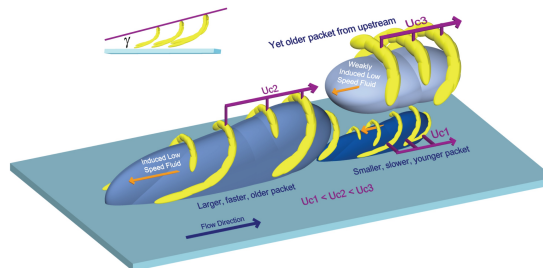


Figure 1.1: Hairpin Packets Proposed by Adrian et al. (2000)

The hairpin packet consists of many hairpin eddies, which are each made up of a horseshoe vortex head and two short counter rotating quasi-streamwise vortex legs. The quasi-streamwise vortices cause low momentum regions by lifting flow away from the wall. The horseshoe vortex

lifts up the surrounding flow and ejects it outward from between the legs of the eddy and immediately behind the hairpin head. Upstream of the vortex, flow rushes downwards, forming a weaker sweep. A stagnation point occurs where the Q2 and Q4 events meet, creating a shear layer. Packets are created when new hairpins are spawned from a mature hairpin as the result of autogeneration, as outlined in Adrian (2007). These packets can create large scale motions (LSM) when several hairpins align in the streamwise direction and travel with the same convective velocity. The hairpins induce a low momentum region between the legs of the vortex, on the order of $2 - 3\delta$. Instantaneous velocity fields obtained from particle image velocimetry (PIV) by Adrian et al. (2000) showed a circular head to the hairpin vortex when plotted in a reference plane moving with the local convective velocity of the structure. The hairpin packets moved with a range of convective velocities, with older, larger packets in the outer boundary layer travelling faster than the new small packets attached to the wall. The hairpin vortices within the packet satisfy some aspects of the attached eddy hypothesis (Townsend 1976), specifically that they grow proportionally to their distance from the wall in both the wall normal and spanwise directions. Hairpin packets are most common in the logarithmic layer, but do grow to span the entire height of the boundary layer. In addition to hairpin packets, there are also larger structures known as very large scale motions (VLSM), an overview of which is given in Smits et al. (2011). These structures are on the order of 10δ and are responsible for a large portion of the turbulent kinetic energy in the flow.

1.2 Thermally Perturbed Boundary Layers

The thermally perturbed boundary layer has been studied in the context of a surface which experiences a sudden change in heat flux. Smits and Wood (1985) highlighted several different studies of such boundary layers in their review paper. Thermal perturbations can consist of a wall under going a sudden step increase or decrease in temperature, as well as an impulsive temperature change. These perturbations behave similarly to small perturbations in surface roughness in that they both produce a new internal layer, defined in the mean sense, within the boundary layer. Immediately downstream of the disturbance in surface heat flux, changes in the boundary layer are contained within a region close to the wall. This region spreads gradually throughout the layer, with the relaxation length defining the distance it takes for the boundary layer to regain self-similarity. Townsend (1961) developed the idea of an equilibrium layer as a location within the boundary layer where production and dissipation of energy are balanced. From this equilibrium, the law of the wall seen in the velocity profile was developed. An analogous derivation can be made for the thermal equilibrium of a boundary layer. If a heat flux is

introduced into the fluid from the boundary, there exists a local equilibrium between the production and dissipation of the mean-square temperature fluctuations. When the heat flux from the surface changes, the local equilibrium is disrupted.

An extensive study by Antonia et al. (1977) examined the case of a cold to hot wall thermal perturbation. The relaxation distance for thermal profiles was found to be in excess of $1000\delta_{\theta_0}$, where δ_{θ_0} was the momentum thickness of the boundary layer at the location of the perturbation. The thermal layer growth rate was found experimentally to be $\delta_T \propto x^{0.8}$, where x is the streamwise distance from the perturbation. Work by Subramanian and Antonia (1981) examined the case of cold to hot change, and found that the growth rate to be slower than the cold to hot cases.

The boundary layer developing over a surface with a small non-zero heat flux allows for heat to be used as a passive contaminant to mark turbulent structures. In order for heat to be considered a passive scalar, several conditions must be met. First, the introduced heat must be small enough for an assumption of neutral buoyancy to hold true. A measure of the buoyancy of a flow is the Richardson number, Ri , which is the ratio of natural to forced convection. When $Ri \ll 1$, the effects of buoyancy are negligible. If the assumption of neutral buoyancy holds, the Reynolds analogy can be used to relate the motion of heat to the momentum within the boundary layer. Reynolds (1874) first suggested that the transfer of heat and momentum are governed by the same turbulent motions. The Prandtl number is the ratio between viscous diffusion and thermal diffusion, and must be close to unity in order for the Reynolds analogy to hold. The Prandtl number is related to the chemical composition of the flow, and for air it is approximately 0.71. A turbulent Prandtl number is defined as the ratio of eddy diffusion for momentum to the eddy diffusion of heat. From an experimental standpoint, Fulachier and Dumas (1976) argued that a flow can be assumed to be neutrally buoyant if the mean, variance, and covariance of the velocity field are unaffected by the introduction of heat.

The use of heat as a tool to study turbulent structures in the boundary layer has been established by several different experimental studies. Fulachier and Dumas (1976) examined temperature and velocity spectra for both a uniformly heated boundary layer and a thermally perturbed boundary layer in order to determine if the Reynolds analogy held for fluctuations in temperature and velocity. A comparison between the two cases revealed that although the mean temperature profiles varied, differences between temperature spectra were negligible. The low wave number temperature spectrum was found to agree well with the u spectrum, while higher wave numbers agreed well with the v spectrum. The experiment examined the viability of using temperature as an indicator of structure by developing a relationship between the temperature spectrum and a velocity spectrum. The temperature spectrum agreed well with a spectrum

consisting of the sum of the three velocity component spectra weighted by their relative energy content. The previously mentioned study by Chen and Blackwelder (1978) used passive heating to draw conclusions about large coherent structures in the boundary layer. This paper outlined the ability of cold fronts to mark the backside of turbulent bulges in the outer boundary layer. Colder temperatures were associated with fluid from outside of the boundary layer, and warmer temperatures originated at the wall. Temperature fronts were observed throughout the boundary layer, strongly associated with internal shear layers. These internal shear layers were later observed in the previously discussed studies of the hairpin packets, being associated with the hairpin heads. Together, these studies suggest that the presence of a cold front in temperature measurements indicates passing of a hairpin vortex.

1.3 Aero-Optical Properties of Turbulence

The speed of light through a fluid changes depending on the index of refraction of the fluid, which is related to its density through the Gladstone-Dale relationship (Gladstone and Dale 1863). Therefore, light passing through a boundary layer with variations in density undergoes distortion due to the varying refraction indices. The interaction of light with the flow is known as the aero-optical problem. The focus of this study is the aero-optical behavior of a turbulent boundary layer. Aero-optics has become increasingly important due to the development in airborne laser systems.

The amount of distortion in a laser signal is measured using the time averaged Strehl ratio, $\bar{S}_t = I/I_0$, where I is the instantaneous intensity of the laser beam and I_0 is the undistorted intensity. The Strehl ratio is related to the wavelength of a specific laser (Smith 1966),

$$\bar{S}_t = \exp \left[- \left(\frac{2\pi OPD_{rms}}{\lambda} \right)^2 \right] \quad (1.5)$$

Here the laser wavelength is λ and OPD_{rms} is the root mean square Optical Path Difference of the light, which is a measure of beam distortion as described below. The wavelength of modern IR and visible light lasers are an order of magnitude smaller than the CO₂ lasers used in the 1960's, causing a significant increase in the distortion of a signal due to turbulence.

Density variations within the boundary layer may arise due to compressibility effect in high speed flows, or temperature fluctuations in the flow. Early studies in aero-optics attempted to relate beam jitter in light traversing the compressible boundary layers to turbulence quantities. In one of the first aero-optical studies, Liepmann (1952) quantified the blurring in Schlieren images by measuring the jitter in a beam of light passing through a compressible flow. A later study by Sutton (1969) developed a "linking equation", which related optical phase variance

to turbulent statistics. A useful way to quantify aero-optical effects is by defining the Optical Path Difference of coherent light as it passes through a boundary layer. The OPD measures the difference between the Optical Path Length (OPL) at a given time and the mean OPL. The OPL is defined as the integral of the index of refraction along the path of beam. Huygen's principle is used to relate the OPL to the deflection angle of a beam of coherent light traversing the boundary layer (Jumper and Fitzgerald 2001). Huygen's principle states that a ray of light travels perpendicular to its associate optical wavefront. This wavefront becomes distorted as it passes through a variable density boundary layer. Therefore, the deflection angle of a small aperture beam of light is related to the spatial derivative of the OPL along the wavefront

$$\theta(x, t) = -\nabla OPL(x, t) \quad (1.6)$$

The deflection angle of the laser in a given direction is therefore the gradient of the OPL in that direction. An important insight into the aero-optical behavior came from Malley et al. (1992), who proposed that the aberrations in the optics caused by turbulent structures also convect. To support this assertion, Malley et al. developed a method of measuring the OPL using the beam jitter resulting from convecting structures and validating the results against the established interferometry methods. Since the optical disturbances are convecting with the turbulence, the change in deflection angle as a function of time can be related to the OPD by applying Taylor's hypothesis of frozen flow to convert the spatial derivative into a temporal derivative. Integrating Equation 1.6 over the entire distorted wavefront and substituting $t = x/U_c$, the OPL can be defined as

$$OPL(x_o, t) = \int_{t_o}^t [-\theta(t)]U_c dt \quad (1.7)$$

An instrument which measured the deflection of a laser beam, called a Malley probe, was created to study wavefront aberrations caused by turbulence (Malley et al. 1992). As outlined in Gordeyev et al. (2003), this instrument was expanded by adding a second laser beam a short distance downstream of the initial beam. The measurement of the deflection angle at the two locations allowed for the mean convective velocity of the aberration to be measured. By cross-correlating the two measurements, the time delay between the two signals is calculated, and the mean convection velocity can be found by dividing the separation between the measurement locations by this value.

The Malley probe was used by Cress et al. (2010) to relate the OPD_{rms} to the flow Mach number, as well as the difference between the surface and the free stream temperatures. Their relationship showed that the OPD_{rms} was directly affected by the temperature difference re-

ardless of the presence of compressibility effects. Work by Gordeyev et al. (2003) used the Malley probe to study subsonic compressible flows and calculated the mean convective velocity of the turbulent structures in the boundary layer to be approximately $0.8U_\infty$. The study also made measurements of mean size of the optical distortions, which were found to on the order of the boundary layer thickness.

The experiments presented here apply the Malley probe techniques used by Gordeyev et al. (2003) to the slightly heated, incompressible boundary layer. A step change in temperature was used to introduce heat as a passive tracer into the zero pressure gradient turbulent boundary layer, allowing for the Malley probe to measure the changing refractive index associated with the passage of turbulent structures. The behavior of the temperature fluctuations and higher moments in the developing internal layer downstream of a sudden decrease in surface temperature was examined in order to relate the temperature distribution to optical disturbances. The mean convective velocity of the convecting optical distortions was examined to determine which turbulent structures were responsible. Temperature and velocity measurements collected at several different wall normal location within the boundary layer were compared to the deflection angle measurements. To determine the location of the structures most responsible for the optical distortion, correlations were taken between the temperature and deflection angle fluctuations as well as velocity and deflection angle fluctuations at various wall normal locations. The size of the structures was examined using the power spectra of the temperature, velocity, and deflection angle fluctuations. The results of this experiment created a better understanding of the aero-optical behavior of coherent structures in the boundary layer and the ability to use that behavior for future boundary layer studies.

Chapter 2

Experimental Setup

2.1 Wind Tunnel Facility

The experiments were conducted in the Merrill Wind Tunnel at the California Institute of Technology. The facility was a closed circuit recirculating wind tunnel with a 2 ft x 2 ft x 8 ft constant area test section and powered by a variable frequency motor, as shown in Figure 2.1.



Figure 2.1: Merrill Wind Tunnel Test Section

The temperature in the test section was controlled by an external controller which adjusted the flow rate of a water-cooled heat exchanger located upstream of the test section in order to maintain a constant temperature. The test section was subjected to a slightly favorable pressure gradient, $dP/dx < 0$, as a result of the constant cross-sectional area along the length of the section. As the flow travelled downstream through the section, the boundary layer displacement thickness increased along the walls and the plate used for the experiment. By the definition of displacement thickness, the effective cross-sectional area was decreasing throughout the length of the section. The resultant pressure gradient was quantified by using an array of static pressure taps on one of the walls of the test section. These taps were located every 4 inches, running the entire streamwise length of the test section. The pressure was measured using a Scanivalve pressure scanner (DSA3217) at 16 of the locations. The first four measurements were spaced 8

inches apart, followed by 7 taps placed at 4 inch intervals, and finally 5 taps placed at 8 inch intervals. The closer spaced pressure taps corresponded to the location in the test section where the boundary layer measurements were conducted. The pressure changes in the test section were described by the acceleration parameter, $K = \frac{-\nu}{\rho U_\infty^2} \frac{dP}{dx} = .67 \times 10^{-6}$, and the change in pressure coefficient, $\Delta C_p \sim -0.1$. The acceleration parameter was the same order of magnitude as those used by DeGraaff and Eaton (2000), and was less than the threshold of $K > 1.6 \times 10^{-6}$ needed to cause deviation from the log law (DeGraaff and Eaton 2000). The free stream temperature for the experiments was held at $T_\infty = 20^\circ\text{C}$, as measured by a thermocouple upstream of the test section. The turbulent boundary layer was studied along the top surface of a plate, described below, 1.04 m downstream of the trip. The flow was first examined at several different Reynolds numbers to establish the Reynolds number independent behavior of the flow within the test section. The Reynolds numbers ranged from $1678 < Re_\theta < 2716$, with the case of $Re_\theta = 1678$ selected for the aero-optical experiments. This Reynolds number corresponded to a free stream velocity of $U_\infty = 9.2 \text{ m/s}$, as measured with a hot wire outside the boundary layer at the given streamwise location.

2.2 Plate setup

The experimental apparatus consisted of a flat plate which was heated internally at two different locations. The plate spanned the length and width of the test section and was tripped with a piece of piano wire along the leading edge. The effectiveness of the trip was verified using the momentum thickness calculation described later. The virtual origin of turbulence was calculated to be 0.994 m upstream of the measurement location, while the trip was located 1.04 m upstream of the measurement location. This suggested that the flow quickly transitioned from laminar to turbulent flow downstream of the trip and was fully turbulent at the point where the experiment was conducted. The plate was divided into 6 different sections, as shown in Figure 2.2

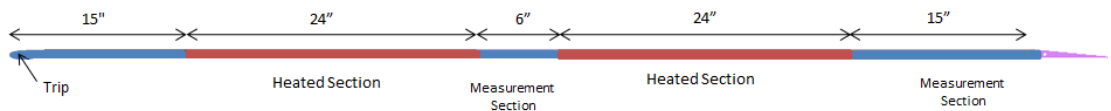


Figure 2.2: Plate Layout

Each section of the plate had an overall thickness of 0.75 in and consisted of several layers. For the first 10 inches in the test section, the plate was unheated solid aluminium, after which the plate became a sandwich design with a 3/16 inch thick nylon insert located between top and bottom aluminium layers. The purpose of this insert was to limit the amount of heat conducted

upstream from the heated section to the unheated section in order to create a step change in surface temperature between sections. The top and bottom surfaces of the plate remained aluminium in order to keep all surface properties except for heat flux consistent.

The heated section of the plate consisted of a 15 in x 24 in flat electric rubber resistance heater (Mod-Tronic Model HRW15X24R24.5L24B-1B) attached to the underside of a 5/16 in thick aluminium plate. The heater had a power output of 540 W and was powered by 115 VAC. The thermal output of the heater was controlled by a Love 16C DIN Temperature Controller and a RTD ribbon sensor (Minco S17624PDZT40B). The RTD sensor was attached directly to the underside of the surface plate, to the side of the heater. Since aluminium is a good heat conductor, with a thermal conductivity of $k = 205 \text{ W/(mK)}$ at 25°C , the surface temperature was assumed to be the same as the temperature of the underside of the plate. This assumption was validated by placing temperature sensors on both sides of the plate and recording the temperatures concurrently. The temperature of the plate could be specified by the controller, but the maximum temperature of the plate was limited by convective heat loss into the boundary layer. The maximum temperature was dependent on the free stream velocity in the tunnel, and the heaters were run at full capacity to set the plate temperature.

The experiment examined the boundary layer growing over the top surface of the plate, although optical equipment passed through both the boundary layers. Since the free stream flow was incompressible and held at a constant temperature, if the underside of the plate was at the ambient free stream temperature, there would be no optical distortion from this boundary layer. As a result, great care was taken to thermally isolate the bottom surface of the plate. The heater was covered with high temperature Mica tape. Air was also used as an insulator. The top plate was separated from the bottom plate by 3/16 in thick nylon inserts placed at each of the section. The rubber heater was only 0.055 in thick, and the remaining space acted as an insulator. The nylon inserts limited heat transfer to the bottom surface, as well as between sections.

Immediately downstream of this heated section was an unheated section where the velocity, temperature, and optical deflection measurements were collected. This section was also aluminium, but contains an acrylic insert to allow for optical measurement, as shown in Figure 2.3. The axis of the 0.5 in diameter acrylic insert was placed 2 in downstream of the end of the heated section. In between the top and bottom plates of this section was another acrylic insert to limit the heat transfer from the surrounding heated sections. There was a second hole 3.0 in downstream of the optical insert to allow for a traverse carrying the hot and cold wire probes. A second heated section, identical in composition to the first, was located on the other side of the measurement section. Downstream of the second heated section was an unheated section with large acrylic inserts that provided for future optical experiments. At the end of the plate,

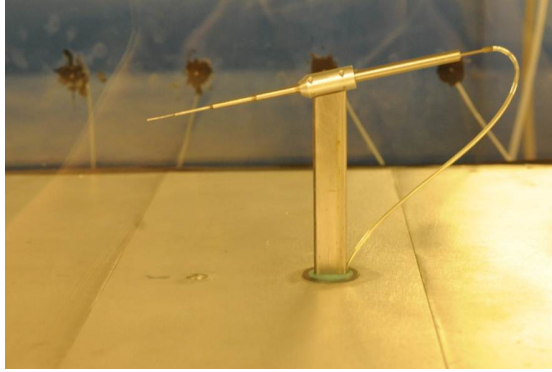


Figure 2.3: Measurement Section with Pitot Tube

there was a symmetrical airfoil flap which was angled upward. The purpose of this flap was to force the location of the stagnation point at the leading edge of the plate to the underside of the plate, preventing interference with the growth of the boundary layer under observation. The plate was secured in the wind tunnel by a set of rails which mounted directly into the frame of the test section and was supported underneath by aluminium columns.

2.3 The Heating System

The surface temperature of the plate was characterized first for the case of no flow. The temperature of the heated sections was limited at 60°C and the heat transfer through the plate was allowed to reach steady state. The heat distribution was first observed using an IR camera (FLIR SC640) as shown in Figure 2.4.

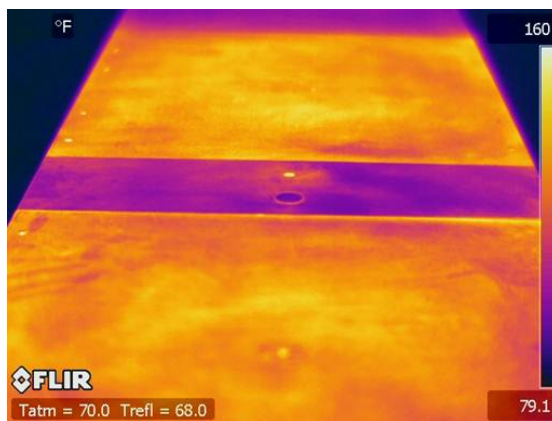


Figure 2.4: Temperature Distribution of Plate from IR Camera, Color bar in $^{\circ}\text{F}$

The IR camera verified that the temperature decrease was close to a step function at the edge of the heated sections and that temperatures in each section were fairly uniform. A more accurate measurement of plate temperature distribution was conducted by taking measurements at different locations on the surface with the RTD probe as seen in Figure 2.5. The measurement

locations are noted in black and the surface temperature is linearly interpolated between these points. The cooler section corresponds to the acrylic section at the end of the plate.

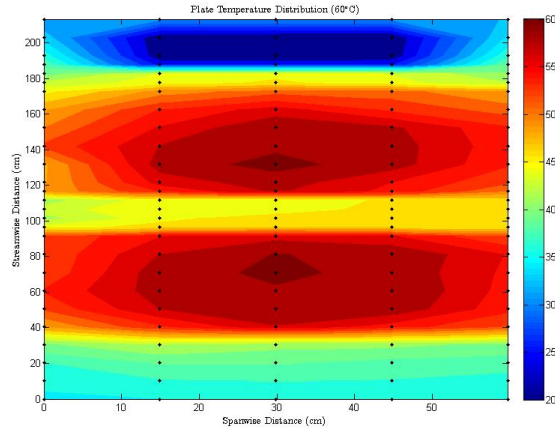


Figure 2.5: Plate Temperature Distribution Obtained by RTD Probe

The upstream plate, Plate 1, had an average temperature of 56.3°C and a standard deviation of 2.9. The downstream plate, Plate 2, had an average temperature of 55.1°C and a standard deviation of 3.4. The middle unheated section had a mean temperature of 45.6°C , with a standard deviation of 1.5. The two heated plates were slightly warmer in the center as a result of conductive heat losses to the unheated sections, and convective heat losses off the sides of the plate. On Plate 1, the average spanwise temperature gradient was $0.19^{\circ}\text{C}/\text{cm}$, and on the Plate 2 it was $0.22^{\circ}\text{C}/\text{cm}$. The average streamwise temperature gradient is seen in Figure 2.6.

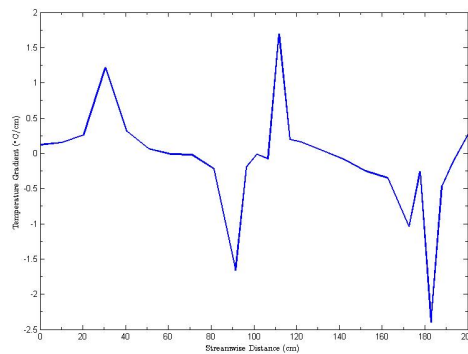


Figure 2.6: Plate Streamwise Temperature Gradient

The beginning of each heated section of the plate was clearly marked by a strong positive temperature gradient, followed by a region of almost constant streamwise temperature. The end of the section was marked by a strong negative temperature gradient.

The steady state temperature of the plate at several different locations was measured when $U_{\infty} = 9.2 \text{ m/s}$. The RTDs for Plates 1 and 2 were located approximately 2 cm upstream and downstream of the step change in surface temperature respectively. The temperature on the

underside of Plate 1 was measured in the center of the plate, approximately 30 cm upstream of the end of the heated section. The temperatures are given in Table 2.1.

Table 2.1: Temperature Characteristics of Experiment

Location	Temperature ($^{\circ}\text{C}$)
T_{∞}	20
Plate 1	44.0
Plate 2	42.8
Underside of Plate 1	27.2
Hot Wire Measurement Location	28.6

2.4 Flow Measurements

Velocity measurements were collected using constant temperature anemometry (CTA) with a platinum plated tungsten probe (Dantec 55P05), which had a wire diameter of $5\ \mu\text{m}$ and a sensing length of 1.25 mm. The frequency response of the anemometer (A.A Labs AN-1005) was measured using the square wave test described in Bruun (1995) and found to be approximately 17 kHz. The anemometer had a built in low-pass filter for $f_c = 14\ \text{kHz}$. The hot wire signals were recorded at $f_s = 30\ \text{kHz}$ and amplified by the anemometer to span the $\pm 10\ \text{V}$ of the National Instruments Data Acquisition Board (NI PCI-6014). The sampling frequency of 30 kHz was chosen to satisfy the Nyquist criteria that the data be sampled at twice the rate of the highest frequencies measured in the flow in order to prevent aliasing. The filter on the anemometer removed any fluctuations above 14 kHz, so the minimum sampling rate needed was 28 kHz. The sampling rate was slightly over twice the Nyquist frequency since the anemometer filter was a low pass filter which tapers off over a range of frequencies. The data acquisition and storage was controlled using LabView. The hot wire probe was mounted on a traverse (Velmex XN10-0040-M01-71) which used a stepping motor (Velmex PK245-01AA) to record the velocity at 31 different logarithmically spaced wall normal locations within the boundary layer. The position of the hot wire was determined using LabView to set the number of turns performed by the traverse, with each turn representing a vertical movement of $2.5\ \mu\text{m}$. The initial height of the probe was set by photographing the probe's position using a telephoto lens. Using a meter stick placed at the same location, the ratio of pixels to millimeters of the photograph was established, and this scale was applied to the initialization photo of the probe. The accuracy of the initial location was on the order of $3\text{E-}4\ \text{m}$. The vertical movement of the traverse had an accuracy of 0.025 mm over 25 cm.

The hot wire probe was calibrated with a Pitot tube measuring the free-stream stagnation

pressure. The Pitot probe was mounted onto the traverse directly above the hot wire during the calibration phase. The probes were placed in the free stream while U_∞ was varied. The Pitot tube measured the velocity by applying Bernoulli's equation between the stagnation pressure in the free stream and the static pressure measured by the static port on the wall of the tunnel at the streamwise measurement location. A fourth-order polynomial was fit to the resulting calibration curve, which was dependent on the free stream temperature. Since the boundary layer was heated, a correction was devised for the calibration curve depending on the local mean temperature at a particular point within the boundary layer. The correction was established by varying the free stream temperature in the tunnel and observing the effects on the velocity calibration curves. The correction was based on the equation specified by Dantec Dynamics in their user guide,

$$V_{correct} = \left(\frac{T_w - T_0}{T_w - T_a} \right)^{.5} * V_a \quad (2.1)$$

Here T_w is the wire temperature, T_a is the local temperature, T_0 is the local temperature used for the voltage calibration curve, and V_a is the measured voltage. T_w was obtained experimentally based on our calibration curves. Several different velocity calibrations were conducted at different free stream temperatures, and a value of T_w was found to collapse the curves onto a common calibration. This correction was based on zero voltage equating to $U_\infty = 0$, so all voltage measurements were first off set by -9.5 V. Both the original and corrected calibration curves are shown in Figure 2.7

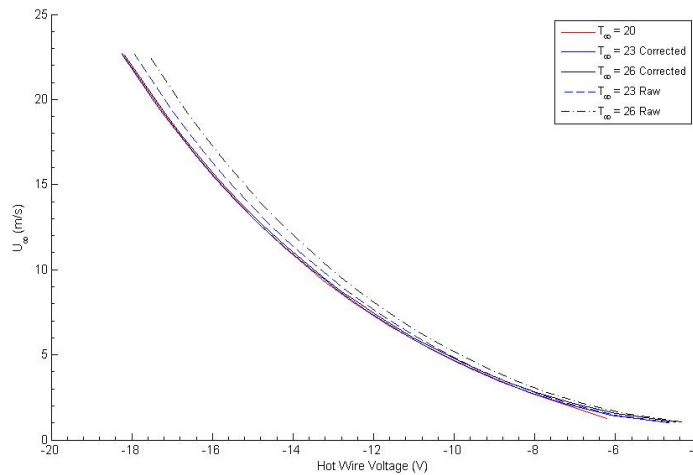


Figure 2.7: Original and Corrected Hot Wire Calibration Curves

The velocity adjustments were based on the mean fluid temperature, so u_{rms} measurements tended to be overestimated. Velocity fluctuations were associated with opposite sign temperature fluctuations since the flow was heated from the plate surface. The cooler fluid originated at the free stream where the velocity was U_∞ , and the warmer fluid originated at the plate surface where

$U_w = 0$. Therefore fluid moving towards the wall was cooler and moving quicker relative to the mean flow around it. Since the instantaneous temperature was less than the mean temperature, the actual velocity was greater than the measured velocity. As a result, the fluctuations were magnified by temperature contamination errors of the hot wire. This error could be corrected if instantaneous temperature measurements were collected along with the velocity measurements, but this would introduce the need to use a triple wire probe, significantly decreasing the spatial resolution of the hot wire data. Only a single normal hot wire was used for this experiment and temperature measurements were taken independently.

The resolution for hot wire measurements depended on the ratio of wire length l to diameter d , l/d , and the viscous length of the wire $l^+ = l * u_\tau / \nu$. In these experiments, $l/d = 250$, which satisfied the condition put forth by Ligrani and Bradshaw (1987) that specified a cutoff of $l/d > 200$ in order to neglect the effects of heat loss to the prongs of the hot wire. In this experiment, $l^+ = 34$, and the effect of the spatial resolution error in l^+ was to decrease the near wall peak of the turbulence intensity (Hutchins et al. 2009). Since errors were already introduced in u_{rms}^+ through temperature contamination, the magnitude of the near wall peak was already subjected to uncertainty. From hot wire spatial resolution errors, using the estimation put forth by Hutchins et al. (2009), the near wall peak increased approximately 30%. Hutchins et al. also determined the effects of hot wire temporal resolutions by examining the maximum flow frequency, $f_c \gtrsim u_\tau^2 / 3\nu$, which for this experiment is ≈ 3.6 kHz. This frequency represents the smallest structure in the flow which contributed to the energy spectrum. Since the cutoff frequency of the anemometer, $f_c = 14$ kHz, was significantly higher than the maximum flow frequency, temporal resolution was not an issue for hot wire probe.

2.5 Temperature Measurements

Temperature measurements were taken at the same 31 wall normal locations as the velocity measurement, using the same traversing system as described in the previous section. The same probe (Dantec 55P05) was used as the hot wire measurements, except the cold wire measurements were taken using Constant Current Anemometry (CCA) as opposed to CTA. The CCA measurements used the same anemometer as the CTA measurements, with the mode switched from constant temperature to constant current. The frequency response of the cold wire was estimated according to the method outlined by Antonia (1981). The cut-off frequency is given by $f_c = 1/2\pi\tau$, where τ is the time constant specified by

$$\tau = \frac{\rho_w c_w d^2}{4k_f N} \quad (2.2)$$

Here ρ_w is the density of the wire, c_w is the specific heat of the wire, d is the wire diameter, k_f is the fluid thermal conductivity, and N is the Reynolds number dependent Nusselt number,

$$N = 0.56Re^{0.45} + 0.24 \quad (2.3)$$

The cut-off frequency for the wire used was fairly low, $f_c = 310$ Hz, but it was similar to those used for other studies using temperature as a passive contaminant, such as the study by Chen and Blackwelder (1978) which had a frequency response of $f_c = 350$ Hz.

The cold wire was calibrated by varying the free stream temperature and relating it to the voltage change measured by the anemometer. Calibration curves were taken at several different U_∞ and found to be unaffected by velocity. This is consistent with CCA run at very low currents, which in this experiment was $I = 0.3$ mA. The calibration curve for temperature, based on five point measurements, is shown in Figure 2.8. The relationship was linear as expected.

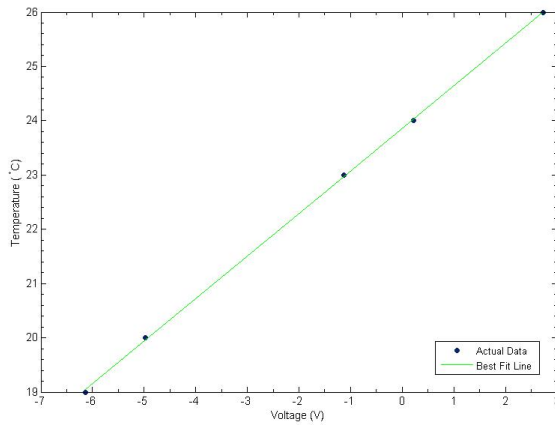


Figure 2.8: Cold Wire Calibration Curve

Temperature measurements were also taken 50 mm upstream of the end of the first heated section in order to establish the temperature profile above the heated plate. The same traverse system was used, but the arm of probe holder was extended to reach over the heated section.

2.6 Malley Probe Measurements

The aero-optical disturbances in the flow related to the density fluctuations in the boundary layer were measured using a Malley Probe. The Malley probe was developed at the University of Notre Dame (Malley et al 1992) and consists of two lasers separated in the streamwise direction, here by 5 mm. The two beams were deflected as they passed through the boundary layer in the wall normal direction and their positions were measured by two position sensing devices (PSD). Figure 2.9 illustrates the basic parts of the Malley probe.

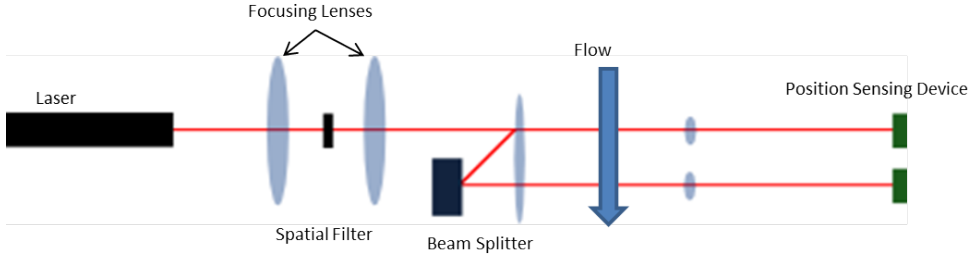


Figure 2.9: Principle Parts of Malley Probe

The deflection angle of the beams was calculated using a focusing lens to transform the small deflection angle into a lateral movement, which was then recorded by the positions sensing devices as shown in Figure 2.10

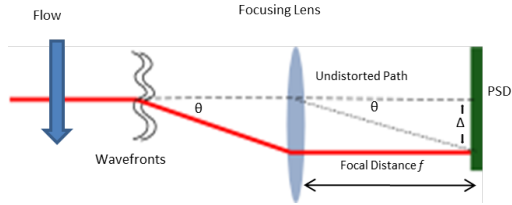


Figure 2.10: Deflection angle calculation

The deflection angle was calculated using small angle approximation as

$$\theta = \Delta/f \quad (2.4)$$

Here Δ is the position of the beam on the PSD photodiode and f is the focal length of the lens. The optical system was set up on a floating optical table underneath the tunnel to isolate the system from mechanical vibrations. The optical setup of the probe is shown in Figure 2.11

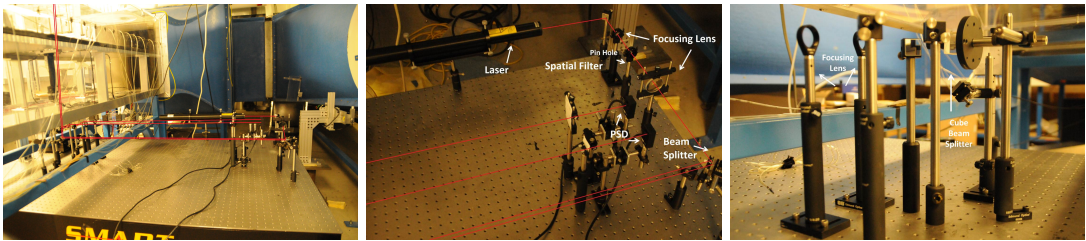


Figure 2.11: Malley Probe Setup

The experiment used a HeNe laser (Edmund Optics NT62-731) with a wavelength $\lambda = 633$ nm and a beam diameter of 1 mm at the measurement location. The laser first passed through a spatial filter which consists of a double convex 25 mm diameter lens with a 100 mm focal length (Edmund Optics 45-892), a 200 μm aperture pinhole lens (Edmund Optics 39-728), and a 50 mm double convex lens with a 150 mm focal length (Edmund Optics 45-907). The spatial filter

removed imperfections in the beam by focusing the beam through a small pinhole, collimating the light. After the spatial filter, the laser was split into two beams by passing through a 12.5 mm diameter, 50R/50T beam splitter (Edmund Optics 45-313). The beam splitter caused half of the beam to turn 90° and the other half of the beam to pass through the lens. A mirror placed 5 mm past the beam splitter was used to turn the second beam 90° , creating two parallel laser beams separated by 5 mm. The beams then encountered another mirror placed directly under the measurement location in the wind tunnel. This mirror reflected the beams at a 90° angle so that they were perpendicular to the surface of the heated plate and aligned such that the two beams were collinear in the streamwise direction. The beams passed through a 50R/50T 30 mm cube beam splitter (Edmund Optics 32-701). The reflected beams from the beam splitter were ignored and travelled away from the Malley probe setup. The transferred beams travelled through the wind tunnel test section, passing through the 0.5 in diameter optical inset in the measurement section of the plate. A flat mirror mounted above the tunnel reflected the beams back along the same path. This second traversing of the boundary layer served to improve the signal to noise ratio of the Malley probe. When the beams passed the cube beam splitter a second time, they were reflected towards another set of mirrors which aligned each beam with its corresponding focusing lens (Thorlabs LB1409-A). These lens had a focal length of 1 m and the position sensing devices were located accordingly.

The position sensing devices (Thorlabs PDP90A) used a photo diode to detect the intensity of light reaching the sensor. The sensor consisted of a photo resistive layer with a common cathode and four anodes corresponding to the quadrants of the sensing surface. Each quadrant produced a measured photocurrent, which was used to find the position of the laser beam. The position sensing devices output $\Delta X = (A + C) - (B + D)$ and $\Delta Y = (A + B) - (C + D)$, where A, B, C, and D were the photocurrents at the anodes. The sum of all the photocurrents was also recorded. The x and y positions of the center of the laser beam intensity was determined as $X = L_x(\Delta X)/2 * SUM$ and $Y = L_y(\Delta Y)/2 * SUM$, where L_x and L_y were the width and height of the sensor surface respectively. The position was relayed through a T-Cube Position Sensor Controller (Thorlabs TQD001) run in open loop mode which returned voltage measurements from ΔX , ΔY , and the voltage sum. The voltage measurements were recorded using the same data acquisition systems as the hot and cold wires. The position measurements were recorded at $f_s = 30$ kHz to match the sampling frequency of the hot and cold wires. These signals were not subjected to an analog filter like the hot and cold wires, but the previously calculated maximum flow frequency of 3.6 kHz for the hot wire indicated that $f_s = 30$ kHz was more than sufficient to capture optical aberrations arising from flow features without aliasing. The position sensing devices were mounted on two linear translation stages (Edmund Optics 38-958) with 0.5 in of

travel in both the x and y directions. The mounting system was used to calibrate the position sensing device while the laser was run with no flow or heating over the plate. The laser was centered on the PSD so that the voltage readings for ΔX and ΔY were zeroed. Then either the x or y position of the PSD was changed in increments of $.025 \pm 0.001$ in until the laser had traversed the entire axis of the sensing surface. The relationship between ΔX and ΔY and voltage was determined for each PSD and then the PSDs were recentered. The calibration curves were linear, as shown in Figure 2.12.

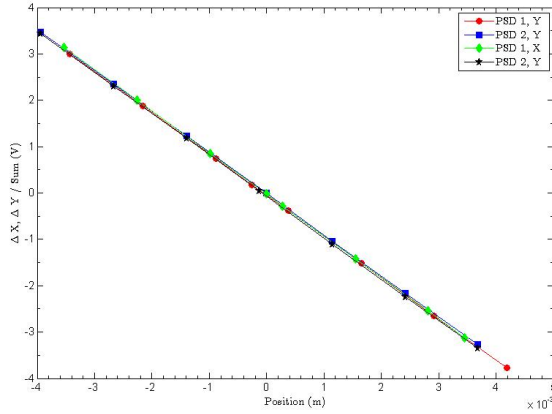


Figure 2.12: PSD Calibration Curves

The upstream position sensing device was defined as PSD 1 and the downstream one was PSD 2. To quantify any effects of electronic noise in the Malley probe, the deflection angle spectrum in the no flow case was examined. The deflection angle spectrum, S_θ , was calculated by recording the deflection angle, θ , as defined in Equation 2.4, as a function of time using LabView and following the Welch method to calculate power spectral density. The raw data was exported into Matlab, where it was sectioned into blocks of 2^{15} data points with 50% overlap between the blocks. The data was then windowed using a Hann window function, $w = 0.5 \left[1 - \cos \left(\frac{2\pi n}{N-1} \right) \right]$, where n is a given data point within the data block and N is the total number of points in the block. The energy density spectrum for each block was calculated as $S_\theta(f) = |\hat{\theta}(f)|^2$, where $\hat{\theta}$ is the Fourier transform of the deflection angle. The deflection angle spectrum for each laser was found by averaging S_θ over all of the blocks. Figure 2.13 shows $S_\theta(f)$ for both of the laser beams in the no flow case.

The power density spectra for the two lasers showed that there was some low frequency noise in the Malley probe, and the energy levels drop off significantly at higher frequencies. This spectrum was important to establish the baseline for the deflection angle spectrum of the heated flow. The Malley probe is an optically sensitive device which had not been used before in this lab, so establishing the no flow case was essential for determining the noise in later measurements.

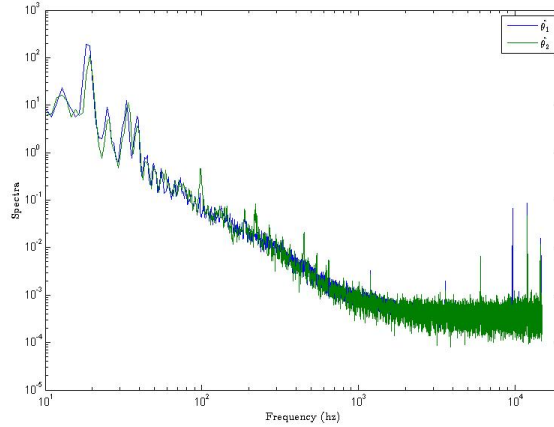


Figure 2.13: Power Density Spectra of Lasers in No Flow Case

2.7 Measurement Locations

The Malley probe was run simultaneously with the hot wire or with the cold wire in the aero-optical experiments. The relative locations of the two lasers and the hot/cold wire probe are shown in Figure 2.14.

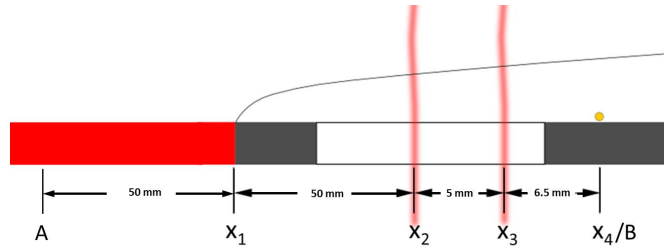


Figure 2.14: Location of Measurements Relative to One Another.

The end of the heated section and the beginning of a new unheated internal layer is shown at location X_1 . The two Malley probe lasers are shown at locations X_2 and X_3 respectively. The hot or cold wire was placed 6.5 mm downstream of the second laser, at location X_4 . To establish the thermal behavior of the flow, temperature measurements were taken independently 50 mm upstream of the Malley probe over the heated plate, at location A. For the temperature comparison between the boundary layer over the heated wall and at X_4 , the downstream measurement location was referred to as location B instead of X_4 .

Chapter 3

Results

3.1 Flow Characteristics

The assumption that the boundary layer behaves as a zero pressure gradient turbulent boundary was verified by examining the velocity statistics for a variety of Reynolds numbers and comparing them to previous zero pressure gradient boundary layer studies, such as those by Örlü (2009). The wall normal profile of the mean flow was plotted in inner coordinates, with both the heated and unheated boundary layers shown for comparison in Fig 3.1 The friction velocity, u_τ was calculated using the Clauser method (Clauser 1956). The wall shear stress, τ_w was found by matching Equation 1.3 to the measured velocity profile in the log region. The value of τ_w was then used for the viscous unit scaling.

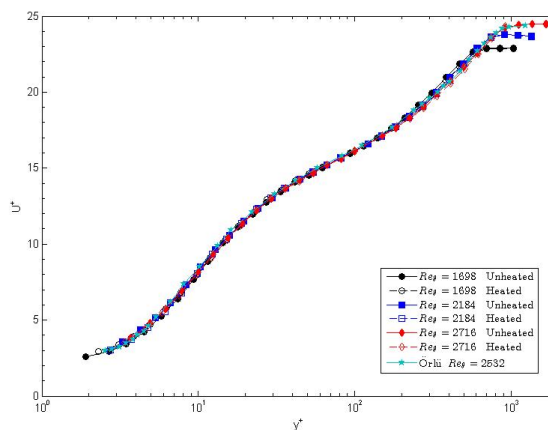


Figure 3.1: Mean Velocity Profile, Inner Scaling

The collapse of the unheated profiles at all Reynolds numbers studied and their agreement with the data from Örlü indicated the assumption of a zero pressure gradient flow was valid. There were no discernible changes between the heated and unheated flows, which supported that

the introduced heat flux from the wall was not altering the flow.

The streamwise turbulence intensities were found for several Reynolds numbers and are shown in Figure 3.2

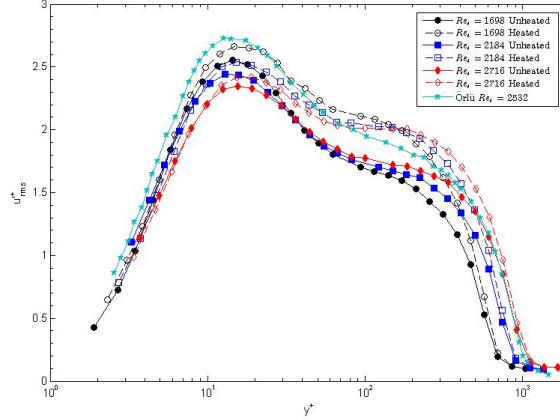


Figure 3.2: Turbulence Intensities

The behavior of the unheated streamwise turbulence intensity agreed with the data from the Örlü experiments, when hot wire resolution was considered. The Örlü experiments had much better spatial resolution, which accounted for the higher turbulence intensities at near wall locations. Evidence of spatial resolution errors in our hot wire data was seen in the near wall peak, which appeared to be decreasing with increasing Reynolds numbers. The decrease was the result of increasingly poorer spatial resolution of the wire as l^+ increased. There was some difference between the heated and unheated turbulence intensities, but this was most likely due to error in the temperature correction of the hot wire, as described previously. The heated turbulence intensities showed the same near wall peak, and followed the same general trend as the unheated intensities. The near wall peak turbulence intensity increased by $\approx 5\%$ for $Re_\theta = 1698$ between the heated and unheated cases, but the deviations were more significant in the outer boundary layer where T'_{rms} was more significant. For $Re_\theta = 1698$, the maximum difference between heated and unheated u'_{rms} occurred at $y^+ = 139$ and was approximately 20%. The other Reynolds numbers had slightly less differences between the two cases. The turbulence intensities were in better agreement even further out in the boundary layer where the T'_{rms} had decreased significantly

The skew and kurtosis of the unheated flow were found for the range of Reynolds numbers and are shown in Figure 3.3. The profiles collapsed as expected and showed good agreement with the zero pressure gradient boundary layer data from Örlü. From these turbulence statistics was it acceptable to consider the boundary layer as a fully developed zero pressure gradient turbulent boundary layer.

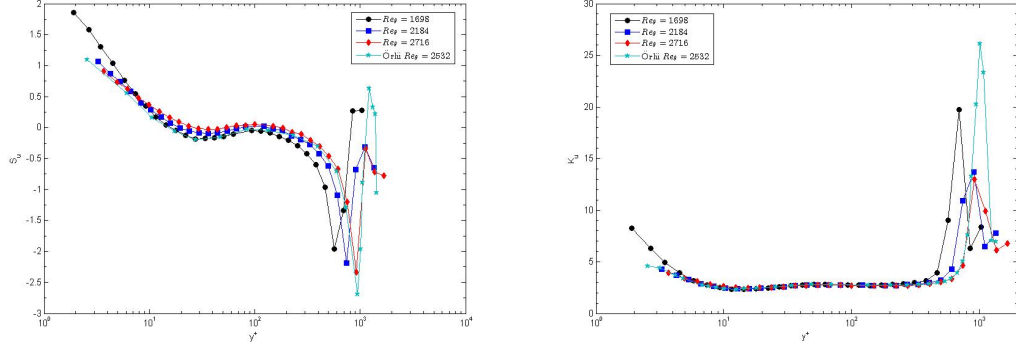


Figure 3.3: Skew and Kurtosis of Velocity

The momentum thickness for the flow conditions and at the location used for the aero-optical experiments was calculated from the mean velocity measurements taken at 31 points within the boundary layer. The measurement location was 1.04 m downstream from the trip, with a free stream velocity of 9.2 m/s, and a Reynolds number based of the momentum thickness, $Re_{\theta} = \frac{\delta_{\theta} U_{\infty}}{\nu} = 1698$. The boundary layer thickness was $\delta = 26.9$ mm, or $\delta^+ = 685$.

Temperature data was taken at two locations in order to establish the growth of the internal thermal layers growing from the leading and trailing edges of the heating section. The mean temperature and temperature fluctuations are shown in Figure 3.4 and Figure 3.5 respectively. The data includes measurements taken 50 mm before the end of the heated section, location A, and at the unheated measurement location where the cold wire measurements were taken simultaneously with the Malley probe measurements, location B. The temperature measurements were non-dimensionalized using a “friction temperature”, $T_{\tau} = q_w / \rho C_p u_{\tau}$, where q_w is the wall heat flux, ρ is the fluid density, C_p is the specific heat capacity of air, and u_{τ} is the local friction velocity. The non-dimensional temperature was calculated as $T^* = (T_{wh} - T) / T_{\tau}$, where T_{wh} is the temperature of the heated wall.

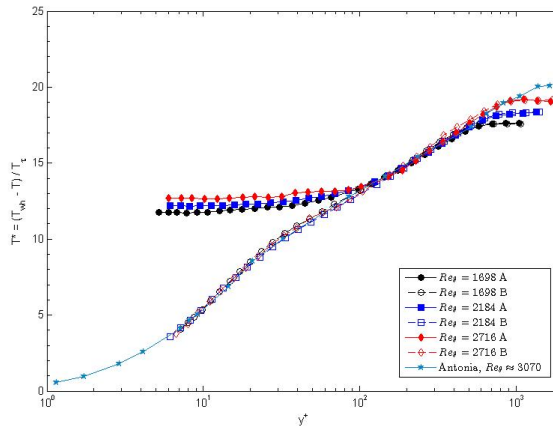


Figure 3.4: Mean Temperature Profiles

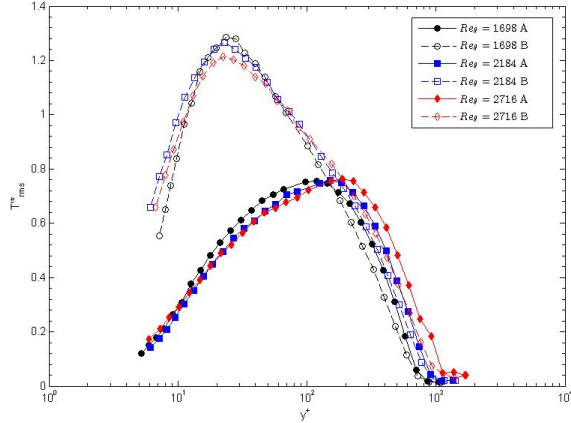


Figure 3.5: Fluctuating Temperature Profiles

The mean temperature profiles over the plate agreed well with the data from Antonia et al. (1977), suggesting that the thermal layer over the plate was well developed. The similarity in shape of both the mean and fluctuating temperatures to the mean velocity and turbulent intensities seen in Figure 3.1 and 3.2 suggests that the heat introduced at the plate's surface was indeed acting as a passive scalar in the flow. The mean temperature profiles from location B collapsed to the temperature profiles at location A at a height of $y^+ \approx 100$, indicating that the thickness of the second internal layer was $\delta_T^+ \approx 100$, or $\delta_T \approx 3.9$ mm at this streamwise location.

The hot/cold wire probe was located downstream of the Malley probe, and both the boundary layer and internal heated layers grew slightly between the measurement locations, as shown in Figure 3.6.

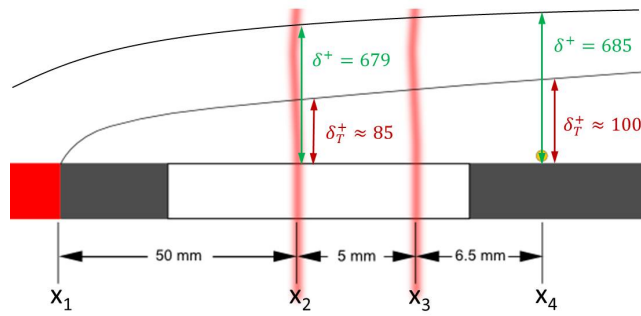


Figure 3.6: Growth in the Boundary Layer and Internal Layer Between Measurement Points

The thickness of the layers at these locations was determined experimentally using the velocity and temperature measurements to find δ_T and δ at X_4 . The previously discussed boundary layer growth rates, $\delta_T \propto x^{0.8}$ (Antonia et al 1977), and $\delta = 0.385x Re_x^{-\frac{1}{5}}$ (Schlichting and Gersten 2004) were applied using the values at X_4 to estimate the thickness at X_2 and X_3 . The overall boundary layer grew from $\delta = 26.7$ mm at X_2 to $\delta = 26.9$ mm at X_4 . The internal

thermal layer grew from $\delta_T = 3.3$ mm or $\delta_T^+ = 84.8$ at $X2$ to $\delta_T = 3.9$ mm or $\delta_T^+ = 100$ at $X4$. The cool internal layer was 12.5% of the entire boundary layer at $X2$ and grew to 14.6% at $X4$.

3.2 Mean Convective Velocity

Temperature fluctuations are concentrated around coherent turbulent structures in a slightly heated flow. The mean convective velocity of the thermally tagged coherent structures in the turbulent boundary layer was found by studying the integral optical effect resulting from temperature changes associated with these structures across the entire boundary layer thickness, using the method outlined by Gordeyev et al (2003). Using Taylor's frozen flow assumption, as well as the idea that optical distortions convect with turbulent structures, the deflection angle of the Malley probe's downstream laser was found in terms of the upstream deflection angle, $\theta_2(t) = \theta_1(t - \tau)$, where τ was the time delay between when a particular coherent structure passed the first beam and when it passed the second. The Fourier transform of θ_2 was then determined as a function of the Fourier transform of θ_1

$$\hat{\theta}_2(\omega) = \hat{\theta}_1 \exp(-i\omega\tau) \quad (3.1)$$

The correlation between of the two deflection angle spectra was then defined as

$$S(\omega) = \frac{1}{T} \langle \hat{\theta}_1(\omega) \hat{\theta}_2^*(\omega) \rangle = \frac{1}{T} \langle \hat{\theta}_1(\omega) [\hat{\theta}_1(\omega) \exp(-i\omega\tau)]^* \rangle \quad (3.2)$$

This spectral cross correlation function can be broken down into its real and imaginary parts, $S(\omega) = \text{Re}(S(\omega)) \exp(i\omega\tau)$, where $\text{Re}(S(\omega)) = \frac{1}{T} \langle \hat{\theta}_1(\omega) \hat{\theta}_1(\omega)^* \rangle$. The time delay which corresponded to the maximum correlation was found using least square estimation of the imaginary part of $S(\omega)$,

$$\min(|\exp(i \text{Arg}[S(\omega)] - i\omega\tau)|^2) \quad (3.3)$$

The minimum of Equation 3.3 was calculated by setting the derivative equal to zero, or

$$\frac{d}{d\omega} \text{Arg}(S(\omega)) = \tau \quad (3.4)$$

Therefore, the time delay was found by plotting the spectral cross-correlation function argument as a function of frequency. Gordeyev et al. found this method to be more robust than a simple cross-correlation of time signals in the presence of low frequency noise. The deflection angle spectra for the two beams are shown in Figure 3.7. In Figure 3.8, the argument of the spectral cross-correlation function is plotted as a function of frequency, with a line representing the

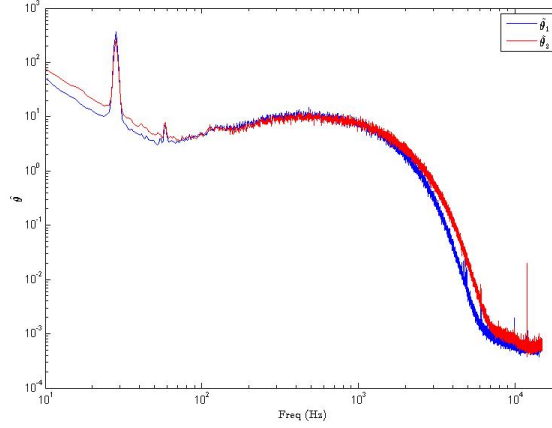


Figure 3.7: Deflection Angle Spectra from the Two Beams

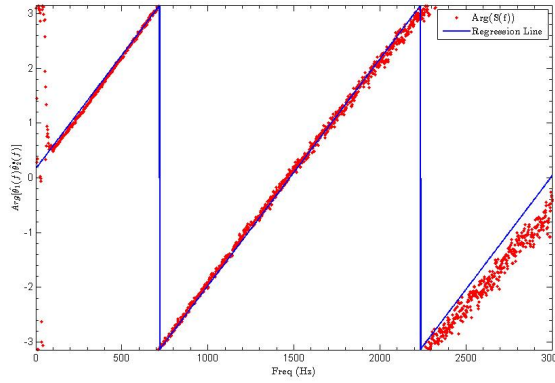


Figure 3.8: Argument of Spectral Correlation Function vs. Frequency

least squares regression line also shown. The time delay calculated from the slope of $Arg(S(\omega))$ between $f = 75$ Hz and $f = 2200$ Hz was 6.59×10^{-4} seconds, which gave a mean convective velocity of $U_c = 7.58$ m/s. When compared to the free stream velocity, $U_c = 0.825U_\infty$. Structures at different locations in the boundary layer have different convective velocities. The value of U_c represents the mean convective velocity over the entire boundary layer, which suggests that the structures that contributed the most to the optical distortion were those centered in the outer boundary layer, where according to Adrian et al (2000) the convective velocity of a coherent structure is approximately $0.8U_\infty$. The study by Gordeyev et al (2003) which used compressibility effects of high speed subsonic flows instead of temperature contamination found a mean convective velocity of $0.8U_\infty$ as well.

The convective velocity was also calculated using the cross-correlation function between the two laser positions,

$$R(\tau) = \frac{\theta_1(t)\theta_2(t + \tau)}{\sqrt{\theta_1^2}\sqrt{\theta_2^2}} \quad (3.5)$$

The correlation between the two beams as a function of time delay is shown in Figure 3.9. The signals were first filtered using a high pass sixth order Butterworth filter with a frequency cutoff $f_c = 70$ Hz in order to remove noise in the signal observed at $f = 29$ Hz and $f = 59$ Hz which dominated the signal otherwise.

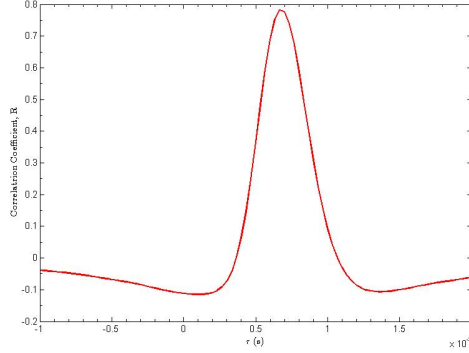


Figure 3.9: Correlation of θ_1 and θ_2

The maximum correlation between the two signals occurred at $\tau = 6.67 \times 10^{-4}$ seconds, with a time resolution of $\Delta\tau = 3.33 \times 10^{-5}$ seconds. Using a non-dimensional time scale, $\tau^+ = \tau * U_\infty / \delta$, where δ is the boundary layer thickness at X4, the time delay was $\tau^+ = 0.228$. This time delay gave a convective velocity of $U_c = 7.50$ m/s, or $U_c = 0.816U_\infty$, which agreed with the values obtained using the spectral cross-correlation function. The two deflection angle signals had a high correlation coefficient of $R = 0.78$, which suggested that the signals were being dominated by coherent structures moving at this convective velocity. If the deflection angle were affected by structures moving at a variety of speeds, the optical aberrations would take different amounts of time to convect past the second laser. This would erode the maximum correlation coefficient as different structures would correspond to different time delays.

3.3 Correlation of Deflection Angle and Flow Properties

The convective velocity and correlation between the two beams suggested that the coherent structures responsible for the optical distortion were located in the outer boundary layer. In order to find a more precise location of the structures responsible, the relationship between the optical disturbances and the temperature and velocity of the flow was examined. The temperature fluctuations from the cold wire were correlated with each beam from the Malley probe. The temperature measurements were taken at discrete locations in the boundary layer as opposed to the beam deflection angle which was the integral of all deflections throughout the boundary layer. The correlation between temperature fluctuation and deflection angle was found at each temperature measurement location and compared to find the location of the maximum

correlation coefficient, as shown in Figure 3.10. The low frequency response of the cold wire, $f_c = 310$ Hz, caused only the larger thermally tagged structures to be recorded by the cold wire, as opposed to the Malley probe measurements which captured all of the structures. Therefore, the relationship in Figure 3.10 was dominated by the correlation between optical variation and the larger structures in the flow. The low frequency response degraded the value of the correlation coefficient, as the Malley probe signal contained information which was not present in the cold wire signal. The hot wire, however, did not suffer from this lower frequency response, and the correlation between velocity and optical response, shown in Figure 3.12, was important to support the correlation in Figure 3.10.

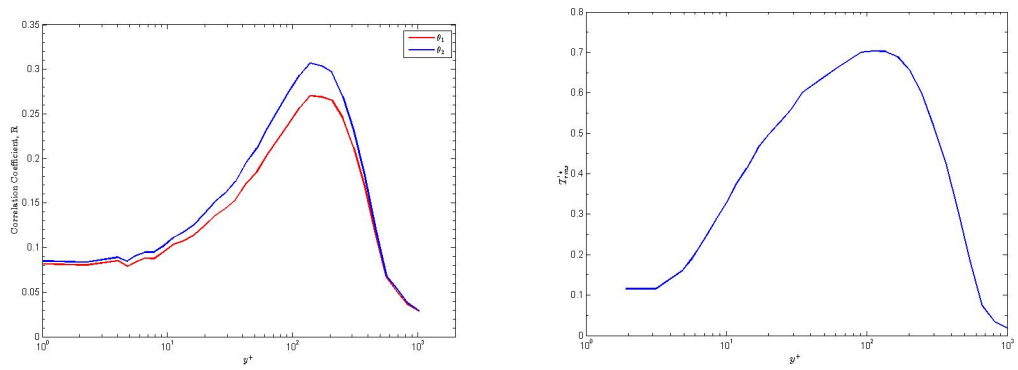


Figure 3.10: (a) Correlation of Temperature and Optical Distortion (b) Temperature Fluctuations

The correlation of θ_2 was stronger than θ_1 because the turbulence was not truly frozen, but rather the coherent structures evolved as they convected downstream. Since θ_2 was closer to the cold wire probe than θ_1 , the turbulent structures in the flow did not have as long to evolve. The maximum correlation coefficient occurred at a height of $y^+ = 139$ for both of the beams. The maximum correlation coefficient for θ_2 was $R = 0.28$, which was small compared to the correlation between the two Malley probe beams, but this was expected as temperature was a point measurement and the deflection angle was an integral. There was a definite peak in the correlation, away from which the correlation coefficient drops off quickly. The peak correlation location was significant when compared to the behavior of the temperature fluctuations, skew, and kurtosis.

The edge of the internal unheated layer was previously established to be located at $y^+ \approx 100$, and the maximum temperature fluctuations occurred just outside of this layer at $y^+ = 114$. The next temperature measurement height was at $y^+ = 139$, which was the location of maximum correlation between temperature and the optical aberrations. This was consistent with the fact that stronger temperature fluctuations cause stronger distortion in optical signals. The skew of the temperature changed signs at $y^+ = 139$ and the minimum of the kurtosis occurred at

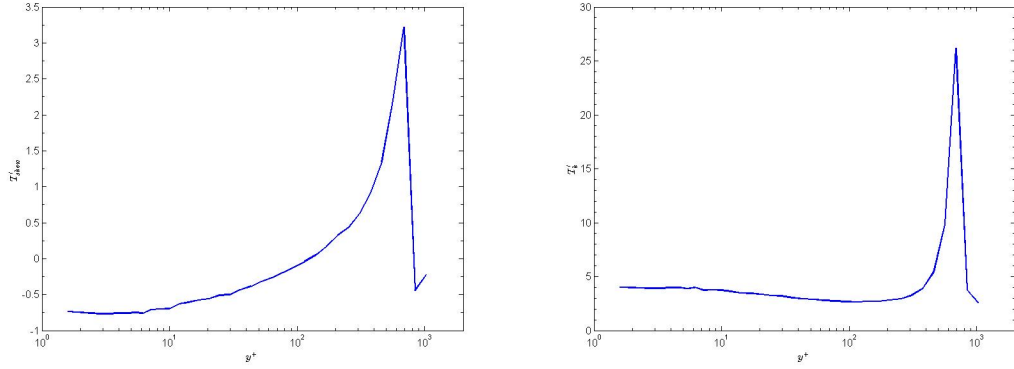


Figure 3.11: (a) Temperature Skew (b) Temperature Kurtosis

$y^+ = 114$. The skew is significant as it indicates that there were equal number of positive and negative temperature fluctuations at this location.

Although temperature was acting as a passive tracer of the velocity field, it was also useful to examine the correlation between the velocity fluctuations and the optical distortions. The temperature fluctuations were believed to highlight these coherent structures as warmer temperatures indicated fluid originating at the wall and cooler temperatures were associated with fluid from the outer boundary layer. The movement of coherent structures transported the fluid to different regions of the boundary layer, causing the temperature fluctuations. The velocity fluctuations were a more direct measurement of coherent structures, although not necessarily the most optically important ones. The velocity measurements were made with a hot wire, which had a frequency response that was much higher than the cold wire. This enabled a wider range of coherent structures to be incorporated into the correlation. The correlation as a function of wall normal location is given in Figure 3.12. The maximum velocity correlation occurred at

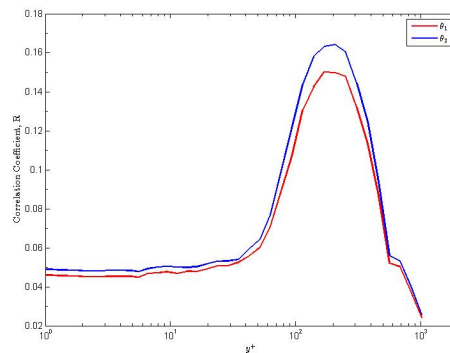


Figure 3.12: Correlation of Velocity and Deflection Angle

$y^+ = 170$, which was one measurement point further from the wall than the maximum found in the temperature correlation coefficient. The correlation coefficient was lower than for the temperature measurements, $R = 0.164$, and the peak was narrower as well. The difference was

not the result of the higher frequency response of the hot wire as opposed to the cold wire, since adding a low pass filter to the velocity signal did not substantially increase the correlation coefficient. The temperature fluctuations were responsible for the optical distortion, not the velocity, so if velocity fluctuations occurred within a region of constant temperature, there was no change in the deflection angle measurement. The temperature fluctuations only traced the velocity field outside of the internal cool layer, and the maximum correlation occurred along the edge of this layer. The wall normal location of the edge was not constant, and as a result, there were regions of constant temperature but fluctuating velocity beyond the defined outer edge of the internal layer. This behavior explains the difference in shape between the temperature and velocity correlation plots. The peak in Figure 3.12 was fairly symmetrical, while the peak in Figure 3.10a was skewed towards the wall. The cool internal layer was effectively blocking the velocity fluctuations from the Malley probe, which could only see the fluctuations which were associated with temperature fluctuations. Therefore the velocity was only significantly correlated with the deflection angle outside of the internal layer, where the temperature and velocity fluctuations were coincident.

The correlation as a function of time delay for the height corresponding to the maximum correlation between deflection angle and temperature is shown in Figure 3.13a, and velocity in Figure 3.13b. The temperature correlation had a large peak at a time delay of $\tau_2^+ = 0.319$ for θ_2 and $\tau_1^+ = 0.546$ for θ_1 . The difference between the time delays was the same as the time delay previously found between the two Malley probe beams. A convective velocity was estimated using the time delay between the temperature fluctuations and the optical distortions. For the first beam, $U_{cT} = 7.03 \text{ m/s} = 0.77U_\infty$, and for the second beam, $U_{cT} = 7.00 \text{ m/s} = 0.76U_\infty$. These convective velocity values were slightly lower than those predicted by the Malley probe, but were within 8% of the value. These results support the idea that the measured temperature fluctuations associated with coherent structures at this location dominated the deflections in the lasers. The convective velocity estimated using the Malley probe only examined the integral effect of the boundary layer, as opposed to examining the flow at a specific point. Therefore, the value of the mean convective velocity from the Malley probe only suggested a location for the structures causing the aberrations, and did not associate the disturbances with a specific structure.

The velocity correlation plot had two peaks of equal magnitude rather than the dominant peak seen in the temperature correlation. For the correlation between the second beam and velocity, the time delays were $\tau_{2a}^+ = 0.160$ and $\tau_{2b}^+ = 0.478$, while the time delays between the first beam and velocity were $\tau_{1a}^+ = 0.376$ and $\tau_{1b}^+ = 0.717$. Averaging the time delays of each beam gave time delays of $\tau_1^+ = 0.319$ and $\tau_2^+ = 0.547$. These time delays were the same as

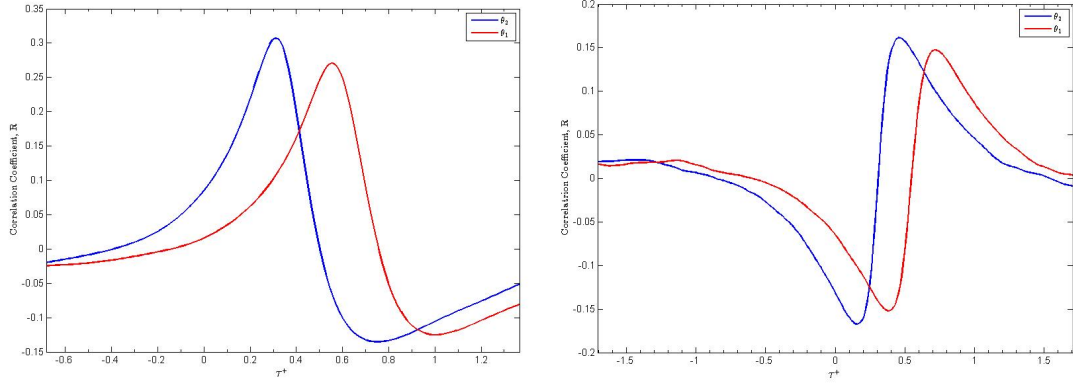


Figure 3.13: Correlation of Deflection Angle and (a) Temperature at $y^+ = 139$ (b) Velocity at $y^+ = 170$

the delays found for the temperature correlations. The average time delay corresponded to the location where the sign of the correlation changed from negative to positive, which suggests that the deflection in the beam was related to the passing of a specific coherent structure. This structure was likely a vortex with a heated core, such as those associated with the heads of hairpin vortices. The streamwise velocity fluctuation on either side of the vortex had a different sign, which accounts for the changing sign of the correlation coefficient. The highest temperature correlation occurred at the center of the structure where the heat was concentrated. The smaller negative correlation peak in the temperature was likely the result of the cooler temperatures associated with the backs of the structures.

3.4 Power Density Spectra

The power density spectra of the velocity, temperature, and optical deflections was examined in order to better understand the scale of the coherent structures causing the aero-optical distortions in the boundary layer. The unfiltered pre-multiplied spectra of temperature fluctuations, streamwise velocity fluctuations, and deflection angle for the downstream Malley probe beam are shown in wave number space in Figure 3.14. The velocity and temperature spectra are for the height $y^+ = 139$. The spectra were normalized by the highest value of each spectrum for easier comparison. The two large peaks in the deflection angle spectrum at low wave numbers were the result of low frequency noise in the measurements.

The peak of the deflection angle spectrum occurred at a larger wave number than either the temperature or velocity spectra. The peak of the velocity spectrum was closer to the deflection angle spectrum, and it was wider than the temperature spectrum. The measured peak in the temperature spectrum was likely too low as the result of the low frequency resolution on the cold wire. The higher frequency structures were not being captured by the cold wire, so the spectrum

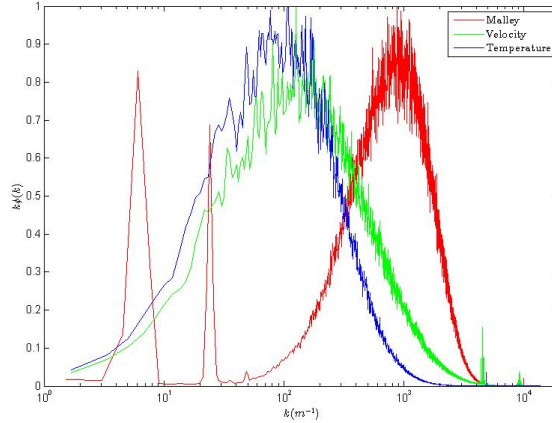


Figure 3.14: Temperature, Velocity, and Deflection Spectra

dropped quickly at the larger wave numbers. The work by Fulachier and Dumas (1976) found that the temperature spectrum peaked at a higher wave number than the streamwise velocity, which was the opposite of what was observed in our experiments. The peak in the temperature spectrum occurred at approximately $f = 110$ Hz, which was lower than the cutoff frequency for the cold wire, although the cutoff point was where the magnitude of the cold wire response had already lost about half of its power. The magnitude of the spectrum would be degraded before the cut off frequency, so it is possible that the peak was lower because of poor frequency resolution. The peak in velocity fluctuations was an order of magnitude below the peak in the deflection angle. Since the velocity spectrum was able to sufficiently capture flow features in the frequency range of the peak deflection angle, the difference between these spectra suggests that the most energetic structures were not responsible for the deflections. Therefore, the relatively low peak in the temperature spectrum may not be caused by the low frequency cutoff of the cold wire.

An examination of the velocity spectra at various heights in the boundary layer showed that the wave number corresponding to the peak in the power spectrum decreased at locations further from the wall. The peak in the temperature spectra initially decreased, but then became relatively constant for locations further from the wall. This trend is an indication that the higher frequencies in the temperature spectrum were being missed. Further from the wall, the size of coherent structures increased, which was seen in the decreasing peak wave number in the velocity spectra. It was expected that the temperature spectra would show a similar trend. The relatively constant peak in the temperature spectra suggests that close to the wall, where the frequency cutoff was lower, the smaller structures were missed.

The spectra of higher moments of both velocity and temperature are shown in Figure 3.16. The higher moment spectra for both velocity and temperature peaked at higher wave num-

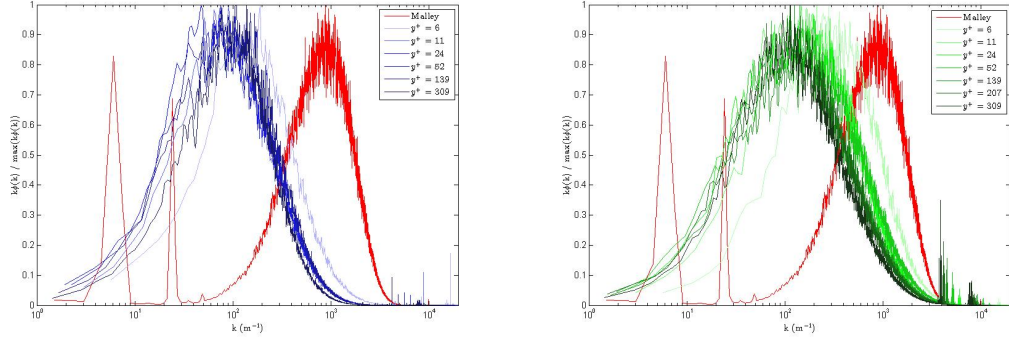


Figure 3.15: Temperature and Velocity Spectra at Different Wall Normal Locations

bers, although the velocity fluctuations showed a much larger increase in wave number than the temperature. The increased wave number suggests that the coherent structures responsible for causing the most significant velocity fluctuations at $y^+ = 139$ were smaller than the most energetic coherent structures in the flow. The wave number associated with the most energetic optical fluctuations indicated the responsible structures were even smaller than those corresponding to the peak energy in the higher order moments of velocity. However, the fourth order velocity fluctuation spectrum was much closer to the deflection angle spectrum than the power spectrum of the velocity.

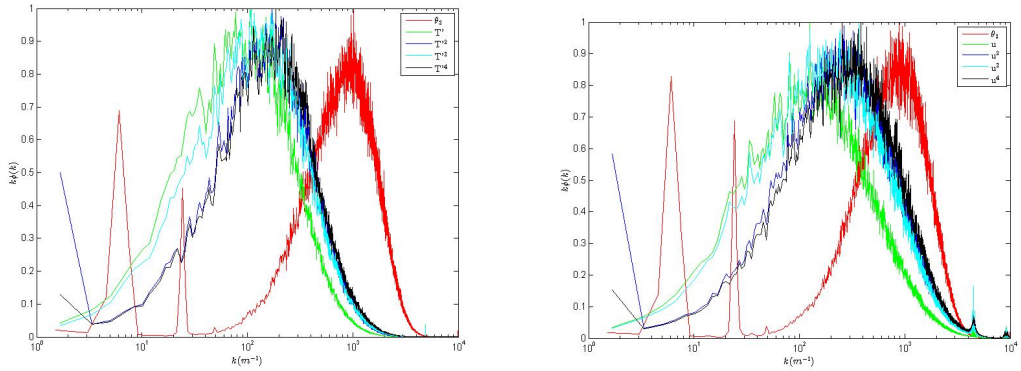


Figure 3.16: Spectra of higher moment fluctuations at $y^+ = 139$ of (a) Temperature (b) Velocity

The discrepancy between the velocity and deflection angle power density spectra gave support to the idea that small vortices in the outer boundary layer were responsible for the optical distortion as opposed to larger scale motions. Structures such as LSM and VLSM are known to contribute significant amounts of turbulent kinetic energy to the flow (Adrian 2007) and occur at much lower wave numbers. Since the deflection angle spectrum peaked at a higher wave number than the velocity spectrum, it can be concluded that the larger scale motions which contribute to the flow were not responsible for the optical distortions. Rather it was likely that smaller vortices which contained a thermally tagged core caused the deflections of the lasers. The size of

the optically most important coherent structures in relation to the boundary layer thickness was seen by plotting the power spectral density of the deflection angle as a function of the Strouhal number, defined as $St_\delta = f\delta/U_c$.

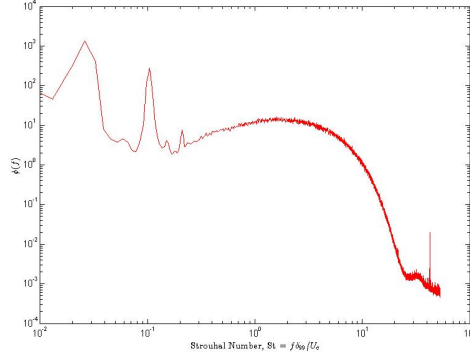


Figure 3.17: Deflection Angle Spectrum vs Strouhal Number

The peak in the spectrum occurred at $St_\delta \sim 1.6$, indicating that the wave number corresponding to peak energy was slightly smaller than, but the same order of magnitude as, the thickness of the boundary layer. Since coherent structures tend to grow in size proportionally to distance from the wall (Adrian 2007), this supports the hypothesis that the Malley probe is being most affected by the structures in the outer boundary layer.

3.5 Conditional Averaging

In order to better understand the behavior of the optical aberrations as they relate to the temperature and velocity fluctuations, the flow was conditionally averaged around the most significant fluctuations in both signals. The thresholds for the signals were set based on the probability density function (PDF) of the temperature and deflection angle fluctuations. The PDF of temperature changed depending on the location of in the boundary layer, as seen in changing values of skew and kurtosis. For the conditional sampling, the PDF used was from the location of maximum temperature fluctuation, $y^+ = 114$. The PDFs for both deflection angle and temperature are shown in Figure 3.18. Only the downstream Malley probe beam was used for conditional averaging because of the very high correlation between the two beams.

The temperature PDF was very close to a normal distribution with $\overline{T'} = 0^\circ\text{C}$, $T'_{rms} = 1.0^\circ\text{C}$, $T'_{skew} = -0.038$, and $T'_{kurt} = 2.7$. For a normal distribution, the skewness is zero and the kurtosis is 3. Therefore, the threshold was chosen to be $|T'| > T'_{rms}$, which corresponds to the highest 17% and the lowest 15% of the temperature fluctuations. The PDF of the deflection angle was skewed, with $\overline{\theta_2} = 0$ mm, $\theta_{2rms} = 0.0033$ mm, $\theta_{2skew} = 0.35$, and $\theta_{2kurt} = 3.9$. Since the signal had a higher kurtosis, the threshold for the deflection angle was set higher, at

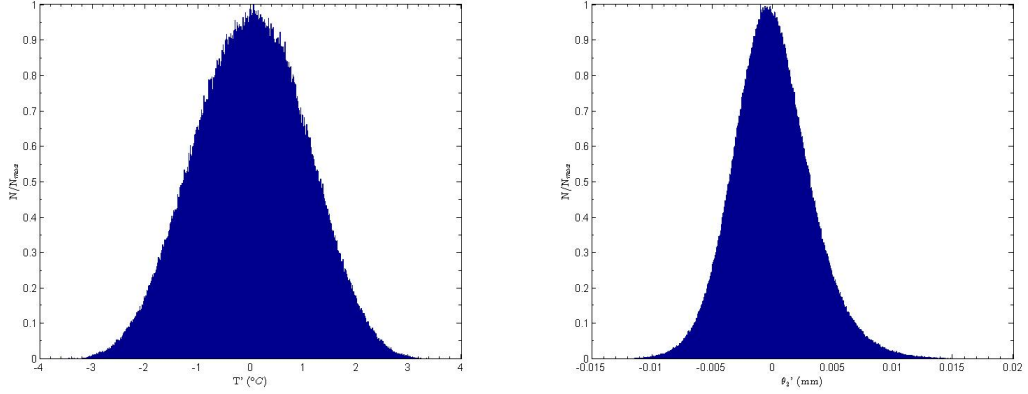


Figure 3.18: PDF of (a) Temperature at $y^+ = 114$ (b) Deflection angle

$|\theta_2| > 2\theta_{2rms}$. This corresponded to the lowest 1.7% and the highest 3.1% of deflections. The gradient of the temperature fluctuations, dT'/dt , is also shown, with $|dT'/dt| > 1.5(dT'/dt)'_{rms}$ highlighted. The deflection angle signals were high pass filtered at $f_c = 70$ Hz, otherwise the noise at low frequencies dominated the time traces. The cold wire signal was not filtered as there was no dominate low frequency noise in this signal.

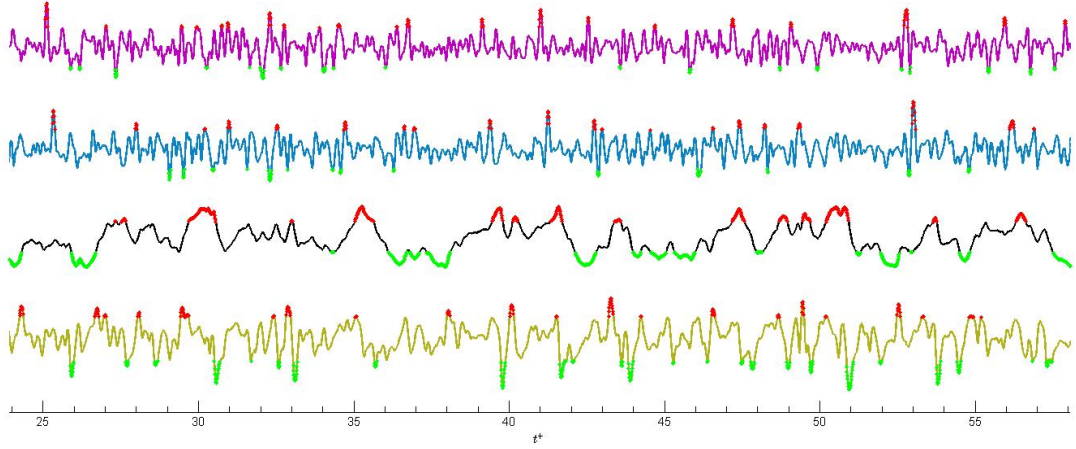


Figure 3.19: Time Traces at $y^+ = 139$; — $T' - \bar{T}$; — $d(T' - \bar{T})$; — θ_1 ; — θ_2 ; • $T' > T'_{rms}$, $dT' > 1.5dT'_{rms}$, $\theta > 2\theta_{rms}$; • $T' < T'_{rms}$, $dT' < 1.5dT'_{rms}$, $\theta < -2\theta_{rms}$

The high deflection angles appeared in several locations to be associated with a high temperature excursion followed by a significant decrease in temperature. Figure 3.19 only shows temperature fluctuations at $y^+ = 139$, which explains why there were some deflections which do not correspond to fluctuations in temperature. The effect of the lower frequency resolution of the cold wire was seen in the time traces, as higher frequency fluctuations were apparent in the deflection angle time trace. This may also explain the presence of significant optical deflections without a corresponding temperature deflection. The temperature fluctuation responsible for

the aberration may have been located at a different height in the boundary layer, or at too high of a frequency to adequately capture with the cold wire. There were also strong temperature fluctuations which were not associated with strong optical disturbances. Many of these were excursions which were below the mean temperature or lasted a significant period of time. There are several possible explanations for these inconsistencies. First, if the temperature was below the mean, the fluid was likely from the outer boundary layer where it was subjected to less intense turbulent fluctuations and was closer to the free stream temperature. Also, optical distortion was related to a change in temperature, so in regions of constant temperature the beam was not distorted until it passed out of that region. Therefore the temperature gradient was examined to determine if the deflections were better associated with the temperature gradient, dT/dt . The gradient was calculate using a centered difference with $dt = 3.33 \times 10^{-4}$ seconds, or $dt^+ = 0.114$, as opposed to the sampling rate of $dt = 3.33 \times 10^{-5}$ seconds, or $dt^+ = 0.0114$. The larger dt was used to filter out the smaller fluctuations and highlight the more significant trends in the temperature gradient. The most significant negative temperature gradients corresponded to high deflection angles, even if the temperature was not high above the mean temperature. These strong $-dT/dt$ events were found mainly to follow behind regions of elevated temperature.

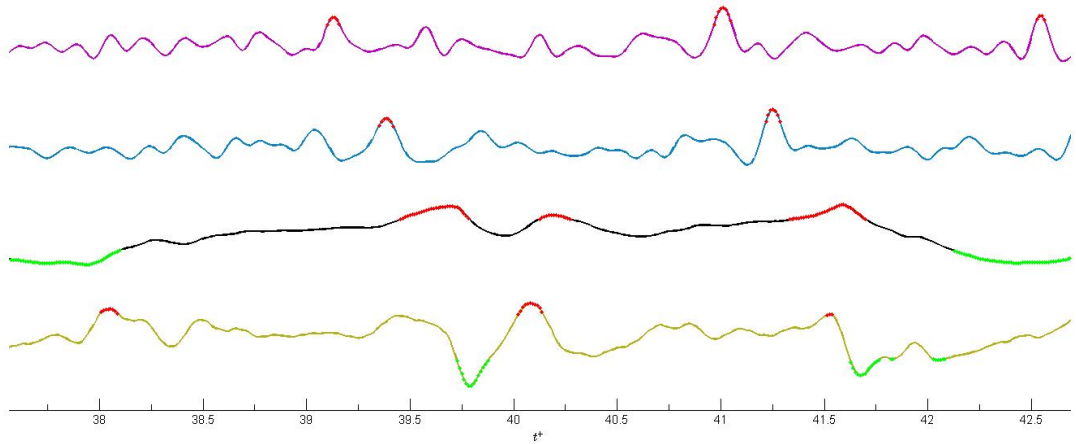


Figure 3.20: Fluctuations of T , dT/dt , θ_1 and θ_2 , symbols same as in Figure 3.19

The time delay between the strong temperature fluctuations and the large deflection angles was found by a closer examination of two of the temperature fluctuations, as seen in Figure 3.20. The first disturbance had $\Delta t^+ = 0.250$ between the two laser deflections and $\Delta t^+ = 0.319$ between the second deflection angle and the maximum temperature excursion. The time delays for the second disturbance in Figure 3.20 were $\Delta t^+ = 0.239$ and $\Delta t^+ = 0.342$ for the deflections and maximum temperature respectively. These values were very close to the time delays estimated from the maximum correlation coefficient, $\tau^+ = 0.228$ and $\tau^+ = 0.319$ seconds.

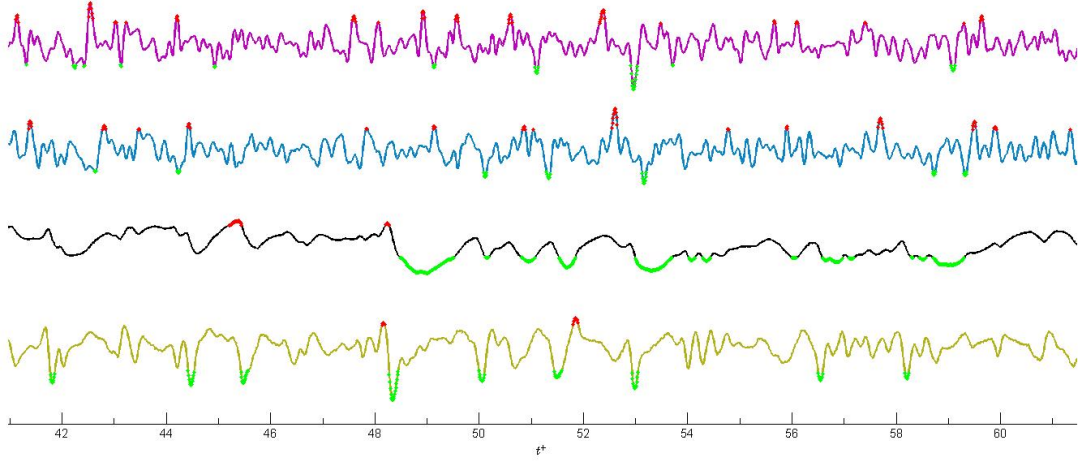


Figure 3.21: Temperature and Deflection Angle Fluctuations at $y^+ = 52$, symbols same as in Figure 3.19

The temperature fluctuations and deflection from the beams was examined closer to the wall, at $y^+ = 52$. The thresholds for the temperature and temperature gradient were the same as at $y^+ = 139$. There were less extreme positive temperature excursions, as expected. There were several locations where there are strong negative temperature gradients associated with the deflection angles. These negative gradients were likely associated with the heated structures passing at higher locations in the boundary layer. This behavior was consistent with the hypothesis of higher temperature fluid concentrated in a hairpin head, with cooler temperatures marking the backside of the structures, which can extend far down into the boundary layer.

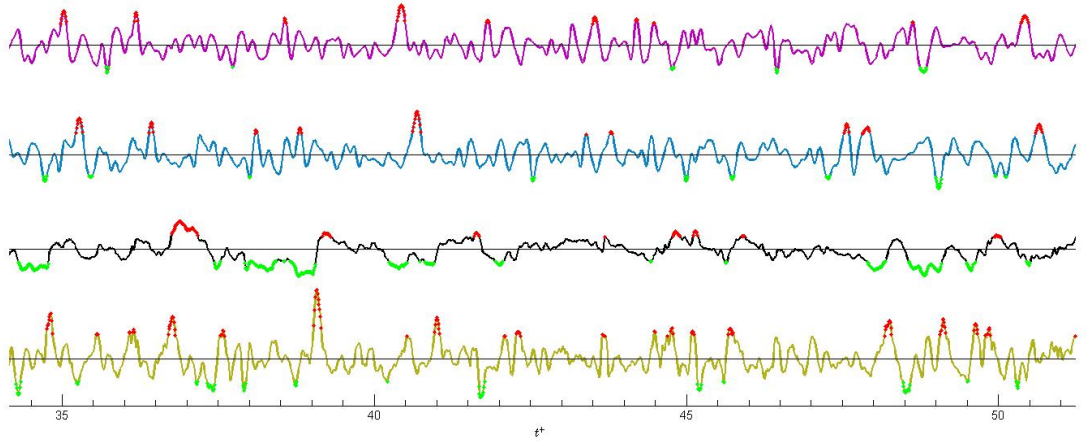


Figure 3.22: Time Traces at $y^+ = 170$; — u ; — du/dt ; — θ_1 ; — θ_2 ; ● $u > u_{rms}$, $du/dt > 1.5(du/dt)_{rms}$, $\theta > 2\theta_{rms}$; ● $u < u_{rms}$, $du/dt < 1.5(du/dt)_{rms}$, $\theta < -2\theta_{rms}$

Time traces of the velocity fluctuations were examined at $y^+ = 170$, or the location of the highest correlation with the deflection angle. The strongest velocity fluctuations were not strongly correlated with the strongest deflection angles, but the velocity gradient appeared to be

better related to the deflections. The presence of a strong deflection was frequently followed by a very strong positive velocity gradient. The average time delay between the maximum deflection and the maximum positive velocity gradient shown in Figure 3.22 between $34.1 < t^+ < 41.0$ was $\Delta t^+ = 0.305$.

The time traces of the velocity fluctuations revealed several sudden step increases in velocity, usually associated with a change in sign. This signature was seen in the velocity deflection correlation coefficient in Figure 3.13b and is consistent with the passing of the head of a hairpin vortex. These results are supported by the analysis of the deflection angle and velocity power spectra, which also suggested the deflections were related to smaller coherent structures in the flow.

Chapter 4

Conclusion

4.1 Main Results

A small amount of heat was used as a passive tracer in order to study the behavior of coherent structures in the boundary layer. Three main diagnostic techniques were used in order to better understand the flow characteristics: the hot wire, cold wire, and Malley probe. The presence of an internal cool layer growing from the end of the heated section allowed the Malley probe to be influenced by the structures in the outer boundary layer. The cooler more uniform temperature region near the wall had less of a degrading effect on the laser of the probe, as the density gradients in this region were weak. The correlations of temperature and velocity with the deflection angle were similar and repeatable for both beams of the Malley probe. Along with the similarity in the boundary layer profiles for velocity and temperature statistics, this behavior suggested that high temperature fluctuations were associated with the presence of a coherent structure. The correlations between the deflection angle of each beam to fluctuations in velocity and temperature demonstrated the ability of the Malley probe to find the heated structures at a particular location in the boundary layer. The maximum correlation between temperature and laser deflection occurred just outside of the internal cool layer, where the temperature fluctuations were the strongest. A mean convective velocity for the coherent structures was found by using the two beams of the Malley probe, as well as the time delay between maximum correlation of the downstream beam and the temperature point measurements at $y^+ = 139$. The convective velocities were similar for both and suggested that the convective velocity measured by the Malley probe corresponded to a structure existing in the outer boundary layer. A comparison of the velocity and temperature correlations, along with conditional averaging of these signals around strong fluctuations suggested that the passing of a thermally tagged coherent structure in the outer boundary layer was responsible for the deflection of the lasers. An analysis of the

deflection angle spectrum showed that the most energetic deflections occurred at higher wave numbers than the most energetic structures in both the velocity and temperature spectra. The peak energy in the velocity spectrum occurred at increasingly higher wave numbers when higher moments of the velocity fluctuations were examined, although still not as high as the peak in the deflection angle spectrum. The most energetic deflections occurred at a Strouhal number $St_\delta \sim O(1)$, which supported the idea that the structures picked out by the Malley probe were indeed the smaller individual vortices in the outer boundary layer. The Malley probe appeared to be an effective tool for passively observing coherent structure in the boundary layer.

4.2 Limitations

There were several significant limitations to this work that need to be overcome before broader conclusions can be made about the coherent structures observed in the boundary layer. The Malley probe was an integral effect, that is, the deflection angle measured was the cumulative result of the laser being deflected by all of the structures it encountered as it traversed the boundary layer. Comparison with temperature and velocity data suggested that the signal was being dominated by a single structure at any given time, but there are several steps that still need to be taken to conclusively state that this is the case. The velocity or temperature at several wall normal locations needs to be found simultaneously with the Malley probe in order to quantify the integral effect on the Malley probe measurements. In addition, the data taken was only collected for a single Reynolds number at a single streamwise location. This introduced some ambiguity into the exact mechanism that determined the location of the most optically significant coherent structures. The relative thickness of the internal layer within the boundary layer changes with streamwise location, or changing Reynolds number. The strongest deflections coincided with the strongest temperature fluctuations, which were located just outside of the internal layer, which for this experiment was in the outer boundary layer. In order to use the Malley probe to study passively heated structures in other flows, it would be necessary to determine the effect of behavior of the internal layer on the deflection angle. The effects of the internal layer thickness on the mean convection velocity of the Malley probe are unknown, but the results agreed with the compressible flow study by Gordeyev et al (2003). This consistency suggests that the thickness of the internal layer does not affect the mean convective velocity, but more tests are needed to confirm that this is indeed true. The results of this experiment suggested that the internal layer effectively filtered out the structures closest to the wall from the Malley probe. There is the potential to study structures at different locations in the boundary layer if the thickness of this internal layer changes which structures dominate the Malley probe. It is

unknown if the outer boundary layer structures will still dominate with a much thinner layer, or if structures closer to the wall will add to the distortion.

The cold wire data suffered from a low frequency cutoff, and as a result, did not effectively capture fluctuations which occurred at frequencies containing the highest energy in the deflection angle spectrum. The hot wire measurements did cover this range and were useful in supporting the temperature data. The velocity measurements included structures which were not strongly heated and did not affect the Malley probe, which was reflected in the lower correlation coefficients between the optical deflections and velocity fluctuations. Also, previous studies by Fulachier and Dumas (1976) have shown that the 1-dimensional streamwise velocity spectrum is not identical to the temperature spectrum. As a result, the differences between the deflection angle, velocity, and temperature spectra could not be accurately attributed to phenomenon such as integral vs. point measurements. A cold wire with a higher frequency cut off would be needed in order to determine any differences between temperature and deflection angle spectra.

4.3 Future Work

The most useful addition to this experiment would be to conduct particle image velocimetry (PIV) immediately upstream of and simultaneously with the cold wire. This would establish a two dimensional, two component velocity field as it relates to the temperature fluctuations and provide a visualization of the structure associated with the cold wire signal. A probe with a thinner diameter wire, and thus a higher frequency cutoff, would resolve the outstanding questions concerning the differences between the temperature and deflection angle spectra. A separate test where the Malley probe is run synchronously with particle image velocimetry would be extremely helpful in quantifying the integral effects of the Malley probe. The PIV field would illuminate structure throughout the entire thickness of the boundary layer at a given instant, which could then be related to the deflection in the Malley probe. If multiple structures are affecting the deflection, these effects should be able to be determined from the coherent structures visualized in the PIV velocity fields. Once these issues are resolved, the Malley probe can be used to draw some conclusions about the structure of turbulence in the outer boundary layer. Boundary layer manipulations such as varying surface roughness could then be studied to try to reduce the optical aberrations that result from turbulence.

Bibliography

- [Adrian et al., 2000] Adrian, R., Meinhart, C., and Tomkins, C. (2000). Vortex organization in the outer region of the turbulent boundary layer. *J. Fluid Mech.*, 422(1):1–54.
- [Adrian, 2007] Adrian, R. J. (2007). Hairpin vortex organization in wall turbulence. *Phys. Fluids*, 19:041301.
- [Antonia et al., 1977] Antonia, R., Danh, H., and Prabhu, A. (1977). Response of a turbulent boundary layer to a step change in surface heat flux. *J. Fluid Mech.*, 80:153–177.
- [Bogard and Tiederman, 1986] Bogard, D. and Tiederman, W. (1986). Burst detection with single-point velocity measurements. *J. Fluid Mech.*, 162(1):389–413.
- [Cantwell, 1981] Cantwell, B. J. (1981). Organized motion in turbulent flow. *Annu. Rev. Fluid Mech.*, 13(1):457–515.
- [Chen and Blackwelder, 1978] Chen, C.-H. P. and Blackwelder, R. F. (1978). Large-scale motion in a turbulent boundary layer: a study using temperature contamination. *J. Fluid Mech.*, 89(01):1–31.
- [Clauser, 1956] Clauser, F. H. (1956). The turbulent boundary layer. *Advances in applied mechanics*, 4:1–51.
- [Coles, 1956] Coles, D. (1956). The law of the wake in the turbulent boundary layer. *J. Fluid Mech.*, 1(02):191–226.
- [Cress et al., 2010] Cress, J., Gordeyev, S., and Jumper, E. J. (2010). Aero-optical measurements in a heated, subsonic, turbulent boundary layer. In *48th Aerospace Science Meeting and Exhibit, Orlando, FL*, pages 4–7.
- [Da Vinci and Suh, 2009] Da Vinci, L. and Suh, H. A. (2009). *Leonardo’s Notebooks*, pages 164–165. Black Dog and Leventhal Pub.
- [De Graaff and Eaton, 2000] De Graaff, D. B. and Eaton, J. K. (2000). Reynolds-number scaling of the flat-plate turbulent boundary layer. *J. Fluid Mech.*, 422(1):319–346.

- [Falco, 1977] Falco, R. (1977). Coherent motions in the outer region of turbulent boundary layers. *Phys. Fluids*, 20(10):S124–S132.
- [Fulachier and Dumas, 1976] Fulachier, L. and Dumas, R. (1976). Spectral analogy between temperature and velocity fluctuations in a turbulent boundary layer. *J. Fluid Mech.*, 77(2):257–277.
- [Gladstone and Dale, 1863] Gladstone, J. H. and Dale, T. (1863). Researches on the refraction, dispersion, and sensitiveness of liquids. *Philos. Trans. R. Soc. Lond. A*, 153:317–343.
- [Gordeyev et al., 2003] Gordeyev, S., Jumper, E. J., Ng, T. T., and Cain, A. (2003). Aero-optical characteristics of compressible, subsonic turbulent boundary layers. *34th AIAA Plasmasdynamics and Lasers Conference*, AIAA-2003-3606.
- [Hutchins et al., 2009] Hutchins, N., Nickels, T., Marusic, I., and Chong, M. (2009). Hot-wire spatial resolution issues in wall-bounded turbulence. *J. Fluid Mech.*, 635:103.
- [Jørgensen, 2002] Jørgensen, F. E. (2002). *How to Measure Turbulence with Hot-Wire Anemometers - A Practical Guide*. Dantec Dynamics.
- [Jumper and Fitzgerald, 2001] Jumper, E. J. and Fitzgerald, E. J. (2001). Recent advances in aero-optics. *Prog. Aerospace Sci.*, 37(3):299–339.
- [Liepmann, 1952] Liepmann, H. (1952). Deflection and diffusion of a light ray passing through a boundary layer. *Douglas Aircraft Company Report SM-14397, Santa Monica, CA*.
- [Malley et al., 1992] Malley, M. M., Sutton, G. W., and Kincheloe, N. (1992). Beam-jitter measurements of turbulent aero-optical path differences. *Appl. Optics*, 31(22):4440–4443.
- [Nagib et al., 2007] Nagib, H. M., Chauhan, K. A., Monkewitz, P. A., Nagib, H. M., Chauhan, K. A., and Monkewitz, P. A. (2007). Approach to an asymptotic state for zero pressure gradient turbulent boundary layers. *Philos. Trans. R. Soc. A*, 365(1852):755–770.
- [Prandtl, 1904] Prandtl, L. (1904). Über flüssigkeitsbewegung bei sehr kleiner reibung. In *Proceedings of 3rd International Mathematics Congress, Heidelberg*.
- [Reynolds, 1874] Reynolds, O. (1874). On the extent and action of the heating surface for steam boilers. *Proc. Manchester Lit. Phil. Soc.*, 14:7–12.
- [Reynolds, 1883] Reynolds, O. (1883). An experimental investigation of the circumstances which determine whether the motion of water shall be direct or sinuous, and of the law of resistance in parallel channels. *Proc. Roy. Soc. Lond.*, 35(224-226):84–99.

- [Robinson, 1991] Robinson, S. K. (1991). Coherent motions in the turbulent boundary layer. *Annu. Rev. Fluid Mech.*, 23(1):601–639.
- [Schlichting and Gersten, 2004] Schlichting, H. and Gersten, K. (2004). *Boundary-layer theory*. Springer.
- [Smith, 1966] Smith, W. J. (1966). *Modern Optical Engineering: the Design of Optical Systems, Optical and Electro-Optical Engineering Series*, chapter 3, pages 49–71. McGraw-Hill, New York, NY.
- [Smits and Wood, 1985] Smits, A. and Wood, D. (1985). The response of turbulent boundary layers to sudden perturbations. *Annu. Rev. Fluid Mech.*, 17(1):321–358.
- [Smits et al., 2011] Smits, A. J., McKeon, B. J., and Marusic, I. (2011). High-reynolds number wall turbulence. *Annu. Rev. Fluid Mech.*, 43:353–375.
- [Subramanian and Antonia, 1981] Subramanian, C. and Antonia, R. (1981). Response of a turbulent boundary layer to a sudden decrease in wall heat flux. *Int. J. Heat Mass Transfer*, 24(10):1641–1647.
- [Sutton, 1969] Sutton, G. (1969). Effect of turbulent fluctuations in an optically active fluid medium. *AIAA Journal*, 7:1737–1743.
- [Tennekes and Lumley, 1972] Tennekes, H. and Lumley, J. L. (1972). *A first course in turbulence*. MIT press.
- [Theodorsen, 1952] Theodorsen, T. (1952). Mechanism of turbulence. In *Proc. 2nd Midwestern Conf. on Fluid Mechanics*, pages 1–19.
- [Townsend, 1961] Townsend, A. (1961). Equilibrium layers and wall turbulence. *J. Fluid Mech.*, 11(1):97–120.
- [Townsend, 1976] Townsend, A. (1976). *The structure of turbulent shear flow*. Cambridge University Press.